

# Deep Graph Neural Networks for Spatiotemporal Forecasting of Sub-Seasonal Sea Ice: A Case Study in Hudson Bay

Zacharie Gousseau<sup>1</sup>, Philippe Lamontagne<sup>2</sup>, and Mohammad Sina Jahangir<sup>3</sup>,  
K. Andrea Scott<sup>4</sup>

<sup>1</sup>Department of Systems Design Engineering, University of Waterloo, Waterloo, Ontario, Canada

<sup>2</sup>Ocean, Coastal and River Engineering Research Centre, National Research Council Canada, Ottawa,  
Ontario, Canada

<sup>3</sup>Department of Civil Engineering, University of Waterloo, Waterloo, Ontario, Canada

<sup>4</sup>Department of Mechanical and Mechatronics Engineering, University of Waterloo, Waterloo, Ontario,  
Canada

## Key Points:

- GraphSIFNet is a sequence-to-sequence model based on the Graph Long-Short Term Memory (GCLSTM) module for sub-seasonal sea ice forecasting.
- The model improves over a statistical baseline in Hudson Bay in short- to medium-term predictions of sea ice concentration.
- GraphSIFNet's graph-based approach provides a more natural representation of sea ice dynamics than those based on 2D kernel convolutions.

---

Corresponding author: Zacharie Gousseau, [zgousseau@uwaterloo.ca](mailto:zgousseau@uwaterloo.ca)

**Abstract**

This study introduces GraphSIFNet (**Graph Sea Ice Forecast neural Network**), a novel graph-based deep learning framework for spatiotemporal sea ice forecasting. GraphSIFNet employs a Graph Long-Short Term Memory (GCLSTM) module within a sequence-to-sequence architecture to predict daily sea ice concentration (SIC) and sea ice presence (SIP) in Hudson Bay over a 90-day time horizon. The use of graph neural networks (GNNs) allows the domain to be discretized into arbitrarily specified meshes, and for more explicit spatial modelling than approaches based on the convolutional neural network (CNN). This study demonstrates the model’s ability to forecast over an irregular mesh with higher spatial resolution near shorelines. The model is trained using atmospheric data from ERA5 and oceanographic data from GLORYS12. Results demonstrate the model’s superior skill over a linear combination of persistence and climatology as a statistical baseline. The model showed skill particularly in short- to medium-term (up to 35 days) SIC forecasts, with a noted reduction in root mean squared error (RMSE) by up to 10% over the statistical baseline during the break-up season, and up to 5% in the freeze-up season. Long-term (up to 90 days) SIP forecasts also showed significant improvements over the baseline, with increases in accuracy of around 10% even at a lead time of 90 days. The study lays the groundwork for future exploration into dynamic graph-based forecasting, the use of more complex graph structures, and forecasting of climate phenomena beyond sea ice.

**Plain Language Summary**

This study introduces GraphSIFNet (**Graph Sea Ice Forecast neural Network**), a novel deep learning framework for predicting sea ice conditions in Hudson Bay. We designed this model to address the challenges of forecasting sea ice concentration (SIC) and sea ice presence (SIP) over a 90-day period. This is important because accurately forecasting sea ice can improve global climate models and support planning and decision-making for activities like shipping and community support in Arctic regions. While previous deep learning methods model sea ice by identifying patterns over a spatial domain divided into a grid structure analogous to images, GraphSIFNet divides the same domain into a set of discrete locations in space called nodes with connections placed between nodes that are close together. The system models the physical interactions between connected nodes, more closely mirroring the way sea ice actually interacts and evolves

51 in nature. Our model shows promising results, improving the accuracy of sea ice fore-  
52 casts, especially during crucial times like the ice melting and forming seasons. Unlike physics-  
53 based systems, GraphSIFNet is entirely data-driven, meaning it can be updated with new  
54 data, enabling it to adapt and remain relevant in the rapidly evolving climate conditions  
55 of the Arctic.

## 56 **1 Introduction**

57 The drastic loss of Arctic sea ice volume is one of the most visible and immediate  
58 impacts of climate change (J. Stroeve & Notz, 2018). The Arctic is the fastest-warming  
59 region on Earth, and this warming is affecting the sea ice cover more than any other com-  
60 ponent of the climate system (Vihma, 2014; J. C. Stroeve et al., 2012; Cavalieri & Parkin-  
61 son, 2012). According to the National Snow and Ice Data Center (NSIDC), Arctic sea  
62 ice extent (SIE)—the total area of the Arctic Ocean with at least 15% ice cover—is see-  
63 ing a steady decline. This is especially prominent in September when sea ice extent is  
64 at its minimum (Serreze & Meier, 2019). Declining sea cover is connected to increasing  
65 air temperatures, changes in atmospheric and oceanic circulation, the albedo feedback  
66 loop, and the concentration of greenhouse gases in the atmosphere (J. C. Stroeve et al.,  
67 2012). The Arctic ice cover is of particular importance as it helps regulate the Earth’s  
68 climate, and the decline in sea ice and subsequent loss of reflectivity directly contribute  
69 to the acceleration of climate change (Moon et al., 2019). Changes in Arctic sea ice cover  
70 also disturb marine and terrestrial ecological dynamics (Post et al., 2013); create chal-  
71 lenges for Northern communities (Meier et al., 2014); and influence human activity as  
72 new trade routes become available through the Arctic (Mudryk et al., 2021). Forecast-  
73 ing sea ice conditions is therefore becoming increasingly important as accurate knowl-  
74 edge of these changes would allow for more effective preparation.

75 In this study, we introduce a deep learning based sea ice forecasting model that em-  
76 ploys Graph Neural Networks (GNNs) integrated within a Long Short-Term Memory (LSTM)  
77 module to predict daily sea ice concentration (SIC) and sea ice presence (SIP) in Hud-  
78 son Bay up to 90 days in advance. The choice of Hudson Bay as our study area is driven  
79 by its important role as a shipping hub, the presence of communities living within the  
80 region relying on maritime re-supply, and its unique characteristics as an in-land sea largely  
81 isolated from the wider Arctic. The 90-day forecasting horizon addresses the needs for  
82 planning and decision-making in industries such as shipping operations as well as the plan-

83 ning requirements of local communities residing in the region. This time horizon cov-  
 84 ers short-term (up to 7 days), medium-term (up to a month) and long-term (up to 3 months)  
 85 planning needs. The study highlights the effectiveness of GNNs in handling irregular spa-  
 86 tial domains by dividing Hudson Bay into a spatially irregular mesh with a higher res-  
 87 olution along shorelines. We evaluate the performance of two types of spatial graph con-  
 88 volutions within the model: the basic Graph Convolutional Network (GCN) and an attention-  
 89 based transformer convolution. The model was trained using sea ice and oceanographic  
 90 data from a coupled ice-ocean reanalysis product (GLORYS12 (Jean-Michel et al., 2021)),  
 91 as well as atmospheric data from the ECMWF Reanalysis v5 (ERA5 (Hersbach et al.,  
 92 2020)). We validate the model’s accuracy by comparing its predictions to a statistical  
 93 baseline and comparing forecasted and observed freeze-up and break-up dates at ports  
 94 on Hudson Bay.

## 95 **2 Background**

96 Sea ice forecasting is a spatiotemporal forecasting task which can be formulated  
 97 as a next-frame prediction problem. Given a sequence of frames  $\mathbf{X} = (\mathbf{X}_{t-n}, \dots, \mathbf{X}_{t-1}, \mathbf{X}_t)$   
 98 with  $\mathbf{X}_t \in \mathbb{R}^{w \times h \times c}$  where  $n$  is the number of frames in the sequence,  $w$  and  $h$  are the  
 99 spatial dimensions of the frames, and  $c$  is the number of channels, the objective is to pre-  
 100 dict the next  $T$  frames in the sequence,  $X_{t+1}, \dots, X_{t+T}$ .

101 While traditional time series modeling techniques such as ARIMA have been widely  
 102 used for forecasting, they are less effective for spatiotemporal forecasting due to their  
 103 inherent limitations in handling spatial dependencies and complex temporal dynamics.  
 104 ARIMA models, primarily designed for univariate time series, lack the capacity to ef-  
 105 fectively model spatial relationships and multi-dimensional data structures, which are  
 106 critical in spatiotemporal forecasting. To address these limitations, methods like Vec-  
 107 tor Autoregression (VAR) (Sims, 1980) and Spatial Autoregressive (SAR) (Anselin, 1988)  
 108 models were developed, offering improved handling of multivariate data and spatial de-  
 109 pendencies, respectively. However, these models still struggled with dynamic spatial re-  
 110 lationships and non-linear interactions. Space-Time Autoregressive Integrated Moving  
 111 Average (STARIMA) models (Pfeifer & Deutsch, 1980) were introduced to better inte-  
 112 grate spatial dependencies with temporal dynamics. Dynamic Linear Models (DLMs)  
 113 and State Space Models (Kalman, 1960) offered a framework for handling evolving tem-  
 114 poral dynamics but were limited in their spatial modeling capabilities.

115 With the advent of deep learning, many neural network methods were developed  
116 for spatiotemporal problems, largely based on spatial convolutions with fixed-size two-  
117 or three-dimensional kernels (Oprea et al., 2022). These convolutional models are par-  
118 ticularly well-suited for image data with a gridded structure such as images or video frames  
119 and allow for learning rich features that are present in real-world image sequences.

120 Graph Neural Networks (GNNs) offer a compelling alternative to Convolutional  
121 Neural Networks (CNNs) for emulating models of physical processes, such as ice dynam-  
122 ics, for several reasons. One of the primary advantages of GNNs in this context is their  
123 inherent ability to capture the spatial relationships between neighboring nodes through  
124 graph edges, which can be arbitrarily specified. This is particularly crucial in applica-  
125 tions like sea ice dynamics, where the spatial relationships are fundamental in determin-  
126 ing heat and momentum exchanges, and other factors influencing ice processes. In GNNs,  
127 both nodes and edges can encode information about the system, and graph convolutions  
128 update these encodings by applying some non-linear function. This allows GNNs to ef-  
129 fectively model the exchange of physical quantities such as heat or ice volume at a given  
130 location in space and time while accounting for the directionality of processes, which is  
131 represented by directed edges. In contrast, CNNs operate on a fundamentally different  
132 principle. They extract features such as edges or gradients from an input image by tun-  
133 ing kernel filters. This process involves convolving these filters over the input image to  
134 identify patterns and features at various scales and orientations. While this approach  
135 is highly effective for tasks like image recognition, where identifying and categorizing vi-  
136 sual patterns is key, it may not be as well-suited for learning the underlying physical laws  
137 that govern interactions between points in space. CNNs typically lack the ability to ex-  
138 plicitly model directional relationships and complex dependencies between disparate points  
139 in a spatial domain, which are critical in understanding and predicting physical phenom-  
140 ena like ice dynamics. A high-level visual representation of these two neural network types,  
141 highlighting their structural and functional differences, is shown in Figure 1. CNNs lever-  
142 age spatial locality and translation invariance inherent in images through convolutional  
143 layers with fixed-size filters that extract local features across the image. Techniques such  
144 as the use of pooling operators, stride convolutions, or dilated filters can be used to cap-  
145 ture longer-range patterns and hierarchical information (K. He et al., 2016; Yu & Koltun,  
146 2016). In contrast, message-passing GNNs can natively capture long-range patterns through  
147 edge propagation, potentially reaching across the entire graph structure given a sufficiently

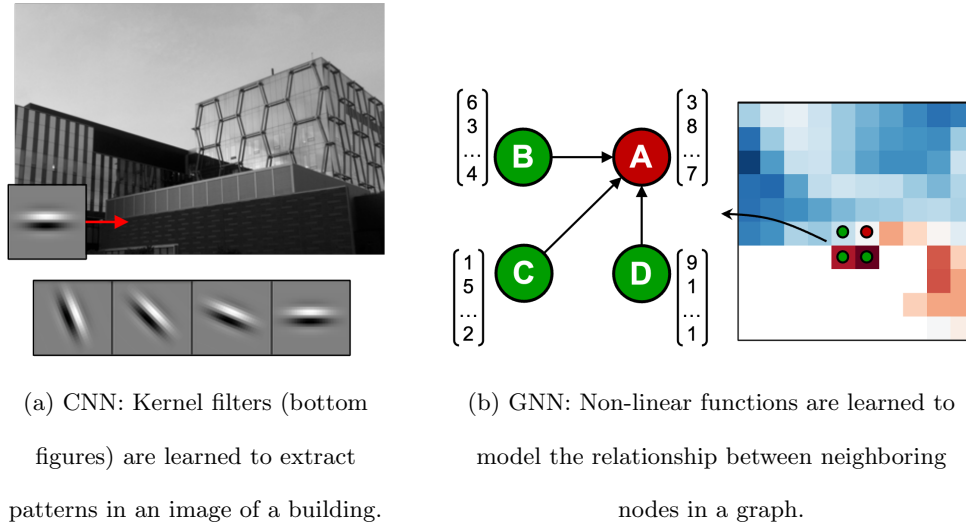


Figure 1: Conceptual comparison of the mechanisms of convolutional neural networks (CNN) and graph neural networks (GNN). (a) CNNs learn kernel filters which slide across the image to identify patterns in the image, such as edges or gradients. (b) GNNs learn a function to update a target node’s state vector (A) by non-linearly combining the state vectors of its neighbours (B, C, D).

148 deep network. Although in most cases the underlying graphs are too large for informa-  
 149 tion to be propagated globally, limited information propagation across can help mod-  
 150 els gain a holistic view of the spatial domain and learn complex spatial patterns (Wu et  
 151 al., 2022). Additionally, most types of GNNs exhibit both translation and rotation in-  
 152 variance as convolutions are applied indiscriminately to all nodes and the aggregation  
 153 operators are most often permutation invariant. Note that this is not always the case;  
 154 operators based on recurrent units such as the LSTM variant of GraphSAGE (Hamilton  
 155 et al., 2017) or sorting units such as the SortPooling aggregator (M. Zhang et al., 2018)  
 156 do not exhibit rotation invariance. Another noteworthy advantage of GNNs over CNNs  
 157 is their scalability due to the inherent parallelism in their architecture, allowing for ef-  
 158 ficient processing of data over large regions or with fine resolution. This parallelism how-  
 159 ever comes at the cost of higher memory usage which may become limiting, though this  
 160 can be circumvented by partitioning the graph and processing the subgraphs indepen-  
 161 dently before combining the outputs. Overlapping subgraphs can be used to ensure no  
 162 spatial artifacts or discontinuities arise from the partitioning.

### 163 **3 Related work**

164 Prior to the advent of deep learning techniques in sea ice forecasting, traditional  
165 physics-based and statistical models were the mainstay for both short-term and long-  
166 term predictions. Dynamic models, often integrated within data assimilation systems,  
167 such as the Pan-Arctic Ice-Ocean Modeling and Assimilation System (PIOMAS) (J. Zhang  
168 & Rothrock, 2003), rely on solving physical equations to simulate the interactions be-  
169 tween sea ice, atmosphere, and ocean. These models are computationally intensive and  
170 require extensive calibration, but are considered fairly reliable due to their capacity to  
171 incorporate well-understood physical processes and parameters. On the other hand, sta-  
172 tistical models such as multiple linear regression (MLR) and autoregressive integrated  
173 moving average (ARIMA) have been used for their simplicity and computational efficiency  
174 relative to physical-based models (Petty et al., 2017). These models often utilize histor-  
175 ical sea ice concentration, temperature, and other meteorological variables to make short-  
176 term forecasts. However, they lack the ability to adequately capture the complex spa-  
177 tial and temporal patterns inherent in sea ice dynamics needed to forecast over longer  
178 timeframes.

179 The application of deep learning techniques to sea ice forecasting has gained in-  
180 creasing attention in recent years due to their computational efficiency and generaliz-  
181 ability, particularly in the face of a changing climate and increased availability of large  
182 training datasets. Early studies applying deep learning to sea ice forecasting were lim-  
183 ited to either spatial or temporal modelling. For instance, Chi and Kim (2017) used a  
184 long-short term memory (LSTM) module to forecast sea ice on a per-pixel level but did  
185 not consider spatial patterns. Kim et al. (2019) later used a deep neural network (DNN)  
186 with two fully-connected layers to forecast sea ice concentration considering interactions  
187 between pixels through dense layers but did not explicitly account for spatial autocor-  
188 relation. Later models based on the convolutional neural network (CNN) were able to  
189 leverage spatial patterns. Andersson et al. (2021) used a U-net trained on both climate  
190 simulation and observation data to forecast monthly sea ice concentration and was found  
191 to out-perform the SEAS5 dynamical model, but did not explicitly model in the tem-  
192 poral dimensions. Spatiotemporal models were then proposed that unify spatial and tem-  
193 poral models. Liu et al. (2021) proposed a model based on the convolutional long-short  
194 term memory (ConvLSTM) (X. Shi et al., 2015) to perform one-step ahead forecasting  
195 of sea ice in the Barents sea which showed promise by outperforming statistical baselines.

196 Asadi et al. (2022) built on this work by proposing a sequence-to-sequence model based  
197 on the ConvLSTM to forecast sea ice presence in Hudson Bay. The model generally out-  
198 performed the European Centre for Medium-Range Weather Forecasts’s (ECMWF) subseasonal-  
199 to-seasonal (S2S) ensemble predictions (Vitart & Robertson, 2018).

200 GNN-based approaches have recently seen some attention in global climate mod-  
201 elling, motivated in part by successes in GNN-based physics simulation models such as  
202 MeshGraphNets (Pfaff et al., 2020) or graph network simulators (Sanchez-Gonzalez et  
203 al., 2020; Rubanova et al., 2022). Keisler (2022) first proposed a GNN for forecasting  
204 the global climate using an autoregressive encoder-processor-decoder architecture. Grid-  
205 ded reanalysis data was encoded onto an icosahedron graph structure on which a message-  
206 passing neural network performed several steps of processing before being decoded back  
207 onto the latitude-longitude grid. Results showed that the model is competitive in com-  
208 parison with state-of-the-art physical models when forecasting geopotential height and  
209 temperature over a 6-day rollout with a 6-hour temporal step. Lam et al. (2022) built  
210 upon this work with GraphCast, a similar model structure with the most notable dif-  
211 ference being the use of multiple icosahedron grids at varying spatial resolution. They  
212 demonstrated greater skill than operational state-of-the-art physical models when fore-  
213 casting global temperature, precipitation, and wind patterns over a 10-day rollout at a  
214 6-hour temporal step.

## 215 **4 Methodology**

### 216 **4.1 Data**

217 In this study, ERA5 reanalysis data is used as atmospheric forcing data to train  
218 the models along with oceanographic variables from the GLORYS12 reanalysis product.  
219 Sea ice concentration estimates from GLORYS12 are used as the target variable and a  
220 proxy for the ground truth.

#### 221 **4.1.1 ERA5**

222 ERA5 (Hersbach et al., 2020) is a climate reanalysis dataset produced by ECMWF  
223 that offers hourly estimates of climatic variables at a spatial resolution of  $0.25^\circ$  from 1979  
224 to present. It is based on the IFS Cycle 41r2 4D-Var data assimilation system and in-  
225 cludes a wide range of climatic variables at different pressure levels of the atmosphere.

226 The IFS system assimilates observations from dozens of satellite missions and ground  
 227 stations to create a physically consistent best representation of atmospheric conditions.  
 228 Although the model does not have a coupled ocean-atmosphere component, it uses daily  
 229 passive microwave-derived sea ice concentration estimates from the Ocean and Sea Ice  
 230 Satellite Application Facilities (OSI-SAF) as boundary conditions (Hersbach et al., 2020).  
 231 In this study, we follow previous studies (Asadi et al., 2022; Andersson et al., 2021) and  
 232 use 2-meter temperature, 10-meter wind speeds, and surface sensible heat fluxes from  
 233 ERA5 as input features to our model (see Table 1)

#### 234 **4.1.2 GLORYS12**

235 GLORYS12 (Jean-Michel et al., 2021) is a global ocean and sea ice reanalysis data  
 236 product developed by the Copernicus Marine Environment Monitoring Service (CMEMS),  
 237 utilizing the LIM2 EVP NEMO 3.1 platform (Madec, n.d.) in the ORCA025 configura-  
 238 tion designed by the DRAKKAR consortium. This configuration includes a global sea-  
 239 ice model with a  $1/4^\circ$  Mercator grid. Atmospheric forcing for the ocean surface model  
 240 is provided by ECMWF’s ERA-Interim (Dee et al., 2011) reanalysis data until 2019, and  
 241 ERA5 data thereafter. The spatial resolution of the ocean and ice models is  $1/12^\circ$ . The  
 242 data assimilation component of GLORYS12 includes in-situ temperature and salinity (T&S)  
 243 profiles, satellite sea surface temperature (SST), and along track sea-level anomalies de-  
 244 rived from satellite altimetry. The assimilation of oceanic observations occurs using a  
 245 reduced-order Kalman filter, which is based on a singular evolutive extended Kalman  
 246 (SEEK) filter. The SEEK filter utilizes a three-dimensional multivariate background er-  
 247 ror covariance matrix and operates on a 7-day assimilation cycle. The system also in-  
 248 tegrates sea ice concentration observations from IFREMER/CERSAT. Historical records  
 249 are available from 1993 to present. This study uses GLORYS12 sea ice concentration,  
 250 thickness, velocities and sea surface temperatures.

#### 251 **4.2 Meshing**

252 Meshes allow for greater flexibility in defining the model’s spatial basis. Unlike two-  
 253 dimensional convolutional approaches, which require defining a regular two-dimensional  
 254 grid of pixels over a region, meshes are comprised of cells of arbitrary sizes, allowing the  
 255 modeler to control which areas are modelled in higher resolution (e.g., around ports or  
 256 passages of interest). Since cells are only defined in regions of interest we also avoid the

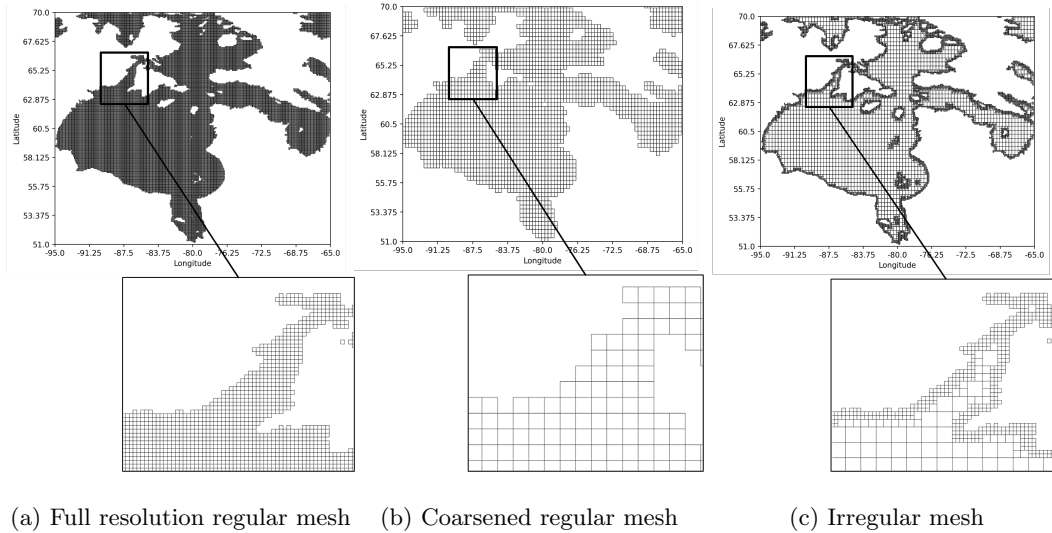


Figure 2: Comparison of different mesh definitions for modeling Hudson Bay. (a) A high-resolution regular mesh with 32,856 cells, computationally intensive but highly detailed; (b) a four-times coarsened regular mesh with 2,425 cells lacking sufficient detail along land interfaces; (c) irregular mesh with 9,422 cells, a compromise for both computational efficiency and high resolution at land interfaces. This approach ensures no cell overlaps land while providing high-resolution data for critical regions like ports, passages, and areas of meteorological interest such as the Kivalliq latent heat polynya.

257 need to apply a land mask as a post-processing step, unlike in CNN-based approaches  
 258 which most often model over the whole region before applying a mask to exclude land  
 259 pixels from the output.

260 Figure 2 shows possible meshes for Hudson Bay using a 1/12 degree grid as the base  
 261 resolution when trying to balance resolution and computational requirements. The mesh  
 262 shown in (a) uses the base resolution as a regular mesh, which is computationally heav-  
 263 ier with its 32,856 cells, while the mesh in (b) uses a regular four-times coarsened ver-  
 264 sion of the same mesh with 2,425 cells, which may not have sufficient definition. At the  
 265 shoreline, this coarse mesh overlaps land but the model does not have the ability to ac-  
 266 knowledge this overlapping. A  $4 \times 4$  cell with only one non-land pixel assigns the sea  
 267 ice concentration value to the entire cell, possibly undermining the model’s ability to rea-  
 268 son about volumetric continuity. As a compromise between resolution and computational  
 269 efficiency, an irregular mesh can be defined with the same four-times coarsened resolu-  
 270 tion refined near shorelines such that no cell overlaps land. This is shown in (c). This  
 271 can be done by recursively splitting the cells of the base (coarsened) mesh in four equal  
 272 parts until no cell overlaps land. The result is a mesh with 9,422 cells. A secondary ad-  
 273 vantage of this technique is that modelling around shorelines at a higher resolution may  
 274 be of interest to port operators or local communities. For shipping and freight purposes  
 275 in Hudson Bay, there is a keen interest in knowing the state of the ice near shipping ports  
 276 since some operations might required ice free conditions. However, large areas of nav-  
 277 igable waters do not require the same high degree of spatial resolution since vessels have  
 278 the possibility to slightly change their routes, thus a coarser resolution is sufficient.

279 To convert gridded data from a grid representation  $X \in \mathbb{R}^{W \times H \times C}$  for data with  
 280  $C$  channels and  $W \times H$  spatial dimensions to a mesh representation  $G \in \mathbb{R}^{C \times N}$  with  
 281  $N$  cells, we first construct a sparse mapping tensor  $M \in \mathbb{R}^{N \times W * H}$  where entry  $(n, p)$   
 282 is assigned 1 if the  $p^{\text{th}}$  pixel of the flattened grid  $Y \in \mathbb{R}^{C \times W * H}$  should be mapped to  
 283 cell  $n$ . We also construct a tensor  $P \in \mathbb{R}^N$  which stores the number of pixels which are  
 284 mapped to each cell. Then, to convert a sample from a grid to a mesh representation,  
 285 for each node we find the mean value of each of its constituent pixels with

$$G = YM^T \oslash P \quad (1)$$

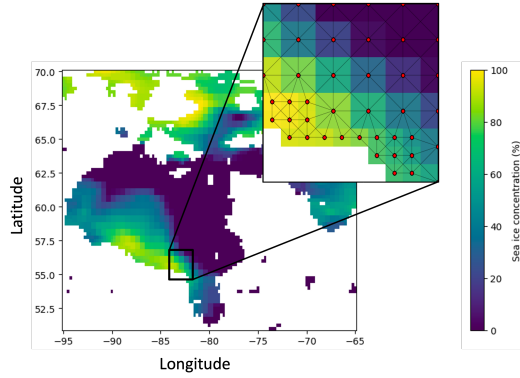


Figure 3: Input images are represented as graphs by relating each neighbouring pixel with edges. In this figure, a spatially irregular mesh is used to represent SIC in Hudson Bay, where red dots represent graph nodes and black lines represent edges.

286 where  $\odot$  represents an element-wise or Hadamard division.  $G$  can be converted back to  
 287 a grid representation by splitting the cells back into its constituent pixels as

$$\hat{Y} = GM. \quad (2)$$

288 Since Equation 1 takes the mean of the constituent pixels of each cell, it cannot be per-  
 289 fectly reverted, instead Equation 2 simply assigns the cell value to each of its constituent  
 290 pixels. Formulating these transformations as matrix multiplications allows for greater  
 291 GPU acceleration which is important if the input meshes are re-meshed dynamically dur-  
 292 ing training, although this is not done in this study.

293 A graph can then be defined based on this mesh by assigning a node to each cell  
 294 and placing edges between any two neighboring cell as in Figure 3. To preserve spatial  
 295 awareness, the positions of each node and size of each cell are added as node features,  
 296 and the length and angle of the edges are stored as edge features. The edges are there-  
 297 fore considered to be directed edges as the edge features are direction-dependent, that  
 298 is, for two nodes  $x_i$  and  $x_j$ , the edge from  $x_i$  to  $x_j$  ( $e_{ij}$ ) is not equivalent to the edge  
 299 from  $x_j$  to  $x_i$  ( $e_{ji}$ )

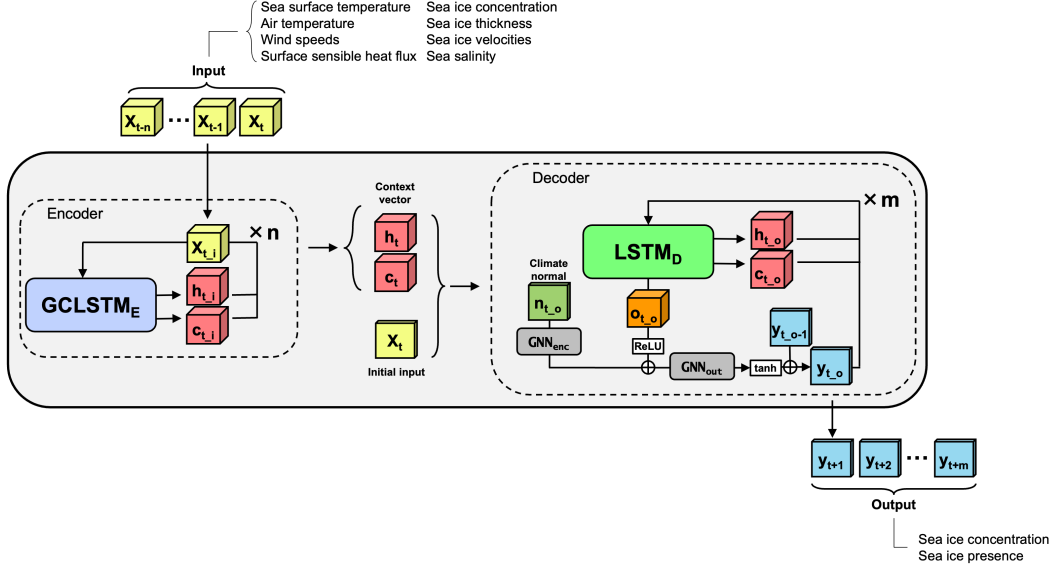
### 300 **4.3 Model Architecture**

301 The proposed model uses graph convolutional long-short term memory (GCLSTM)  
 302 modules within a sequence-to-sequence architecture. The GCLSTM module and the over-  
 303 all architecture are shown in Figure 4, and described in the subsections below.

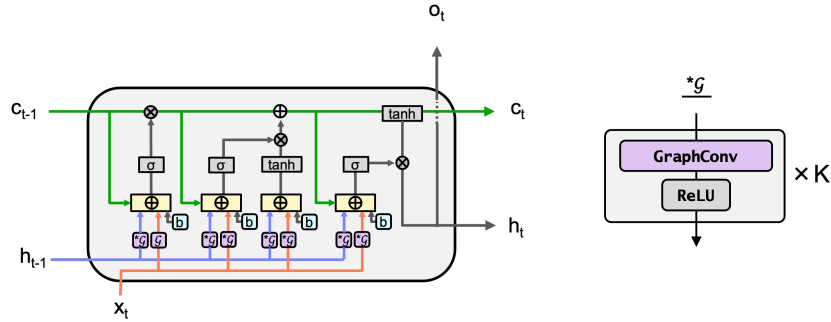
#### 304 **4.3.1 GCLSTM**

305 The graph convolutional long-short term memory (GCLSTM) module used in this  
 306 work is a modified version of the model from Seo et al. (2018), which is in turn inspired  
 307 by the ConvLSTM first proposed by X. Shi et al. (2015). The module closely resembles  
 308 the peephole LSTM introduced by (Gers et al., 2002), with the only modification being  
 309 the addition of graph convolution operators over the hidden and input states at each of  
 310 the input, forget, cell and output gates in the place of weight matrices. This is repre-  
 311 sented as the  $\ast\mathcal{G}$  block in Figure 4b. The graph convolution operators allow information  
 312 exchange between nodes through the directed edges. The model proposed by Seo et al.  
 313 (2018) uses a single Chebyshev graph convolution (M. He et al., n.d.) which has limited  
 314 spatial expressivity since a single convolution can only exchange information between  
 315 immediate neighbors. Since the processes dominating ice formation and break-up are phys-  
 316 ical processes occurring across space, we wish to increase the model’s ability to recog-  
 317 nize spatial patterns, and therefore use  $K$  stacked convolutions followed by leaky ReLU  
 318 activations, which provides information exchange over  $K$  hops. The peephole variant of  
 319 the LSTM is used here as it has been shown to outperform the vanilla LSTM (Joshi et  
 320 al., 2022), particularly for video understanding (Srivastava et al., 2015). The convolu-  
 321 tion operator taking the place of GraphConv in Figure 4b can be arbitrarily selected from  
 322 the myriad graph convolution operators that have been proposed. In this work, we eval-  
 323 uate both the graph transformer convolution from Y. Shi et al. (2021), and the more ba-  
 324 sic Graph Convolutional Network (GCN) first proposed by Kipf and Welling (Kipf & Welling,  
 325 2017).

326 In the graph transformer convolution, the feature vector of a given node  $i$ ,  $x_i$ , is  
 327 updated by aggregating information from its neighbors  $j \in \mathcal{N}(i)$ , and the node itself,  
 328 using edge features from  $i$  to  $j$ ,  $e_{ij}$ . The governing equation for the graph transformer  
 329 convolution is



(a) Overall model architecture. The last hidden ( $h_t$ ) and cell ( $c_t$ ) states of the encoder act as the context vectors and are used as the initial states of the decoder. The encoder learns features from the  $n$  input timesteps, and the last hidden ( $h_t$ ) and cell ( $c_t$ ) states are retained as the context vector used to initiate the decoder, which unrolls over the fixed  $m$  desired output timesteps. The initial input to the decoder  $X_t$  is the ice channel of the last input timestep. GNN<sub>enc</sub> and GNN<sub>out</sub>, used to encode climatology at each output timestep ( $n_{t,o}$ ) and reduce the dimensionality of the output ( $o_{t,o}$ ), respectively, are stacked spatial convolutions with leaky ReLU activations.



(b) Graph convolutional long-short term memory (GCLSTM) module. The module is based on the peephole LSTM (Gers et al., 2002), with the addition of  $K$  stacked graph convolutions applied to both the hidden states and input.

Figure 4: Model architecture showing (a) overall encoder-decoder architecture, and (b) a single graph convolutional long-short term memory (GConvLSTM) cell.  $\oplus$  represents element-wise addition, and  $\otimes$  represents element-wise multiplication.

$$x'_i = W_1 x_i + \sum_{j \in \mathcal{N}(i) \cup i} \alpha_{ij} (W_2 x_j + W_3 e_{ij}) \quad (3)$$

330 where  $\mathcal{N}(i)$  denotes the neighbors of node  $i$ ,  $W$  are weight matrices that project the in-  
 331 puts to their latent representation where the attention coefficients  $\alpha_{ij}$  are given by

$$\alpha_{ij} = \text{softmax} \left( \frac{(W_4 x_i)^T (W_4 x_j + W_3 e_{ij})}{\sqrt{d}} \right) \quad (4)$$

332 .

333 The attention weights allow the model to selectively attend to a given node's neigh-  
 334 bors based on their node and edge feature vectors. The inclusion of edge features and  
 335 an edge specific weight matrix allows the model to learn to relate the edge features to  
 336 better reflect anisotropic evolution of the model state.

337 We compare the transformer convolution with the Graph Convolutional Network  
 338 (GCN) proposed by Kipf and Welling (2017), as it is a commonly used and simpler con-  
 339 volution operator. The GCN operator is defined by the equation

$$x'_i = W^T \sum_{j \in \mathcal{N}(i) \cup i} \frac{e_{ij}}{\sqrt{\hat{d}_j \hat{d}_i}} x_j \quad (5)$$

340 where  $X$  is a weight matrix,  $\hat{d}_i = 1 + \sum_{j \in \mathcal{N}(i)} e_{ij}$  and  $e_{ij}$  are the edge weights from  $i$   
 341 to  $j$ . Since  $e_{ij}$  must be a scalar, here we use the normalized distance between nodes as  
 342 the edge weights. Note that this limits the spatial awareness of the model as it does not  
 343 receive information about the nodes' relative positions, unlike the transformer convolu-  
 344 tion.

### 345 **4.3.2 Sequence-to-Sequence Architecture**

346 The GCLSTM module is used within a sequence-to-sequence encoder-decoder struc-  
 347 ture to learn features from the inputs and evolve the sea ice state forward in time. The  
 348 overall architecture is shown in Figure 4a. Since navigation and offshore operations are  
 349 affected at various degree by the presence and concentration of sea ice, our model fore-  
 350 casts both SIC and SIP as a multi-task learning approach. Although sea ice presence—defined  
 351 as any pixel where SIC is greater than 15%—can be derived from the forecasted SIC val-  
 352 ues, a model trained without the secondary SIP forecasts would not be optimized for this  
 353 15% threshold. It was also found through experimentation that including SIP as a sec-  
 354 ondary task improved SIC forecasts in the break-up and freeze-up seasons.

355 The encoder is responsible for learning rich spatiotemporal features from the in-  
 356 put sequence while the decoder is responsible for evolving the state forward in time from  
 357 these learned features. The encoder therefore acts as an information bottleneck, mean-  
 358 ing it is crucial that the encoder is sophisticated enough to distill the inputs into a con-  
 359 text vector with sufficient information for the decoder to use in the unrolling process.  
 360 Given a sufficiently rich context vector, the decoder does not necessarily need to learn  
 361 additional spatial features within the context vector, nor during the unrolling process.  
 362 Therefore, in this work we use a spatiotemporal GCLSTM module in the encoder block,  
 363 and a simple LSTM in the decoder block. Although the decoder block also contains graph  
 364 convolutions (e.g., in  $GNN_{out}$ ), the distinction between the two is that the GCLSTM  
 365 in the encoder block integrates graph convolutions within the temporal model allowing  
 366 for simultaneous spatial and temporal modelling, while the decoder block models tem-  
 367 poral and spatial dynamics separately, with  $GNN_{out}$  being used mainly for dimension-  
 368 ality reduction. Using an LSTM rather than a GCLSTM module in the decoder block  
 369 also greatly reduces training time in the case where there are fewer input timesteps than  
 370 output timesteps. Note that experiments with a GCLSTM in the decoder were also run  
 371 but showed no improvements over using an LSTM.

372 The encoder processes each input timestep sequentially, updating the hidden and  
 373 cell states at each timestep with layer normalization (Ba et al., 2016) applied to the hid-  
 374 den and cell states after each timestep to increase model stability. The final hidden and  
 375 cell states are the high-dimensional vectors that are taken as the context vectors that  
 376 contain the learned features from the input and are used to initialize the hidden and cell  
 377 state of the decoder. The last input ice state is used as the initial input to the decoder  
 378 (or start token) since we wish to evolve the state forward from this initial state. The de-  
 379 coder is run recurrently for the desired number of output timesteps in a similar fashion  
 380 to the encoder but using the last step’s prediction ( $y_{t-1}$ ) as the input for the current step  
 381 ( $y_t$ ).

382 Since sea ice is highly seasonal, the model is susceptible to a form of modal collapse  
 383 wherein the model converges to a local minimum, predicting only the average sea ice con-  
 384 ditions for a particular day of the year. These daily averages are known as the climate  
 385 normals or climatology. For long-term forecasting of climatological variables, climatol-  
 386 ogy can perform reasonably well compared to dynamic or statistical models due to strong  
 387 seasonality. Since we wish to outperform climatology and expect the model to learn to

388 use it as a heuristic, we choose to include it as an input such that model can focus on  
 389 learning departures from normal conditions. This was shown to be beneficial for sea ice  
 390 forecasting in a previous study (Asadi et al., 2022). Climate normals are calculated as  
 391 the mean ice concentration values for each day of the year over the entire training set  
 392 and are encoded into latent space using a shallow multi-layer GNN before being com-  
 393 bined with the decoder output by element-wise addition. The result is then fed through  
 394 a multi-layer GNN with leaky ReLU activations to reduce the dimensionality to two, and  
 395 finally through a hyperbolic tangent activation to map the values between -1 and 1. This  
 396 output represents the change in sea ice conditions and is added to the last timestep’s pre-  
 397 diction. Since both SIC and SIP should be bound between 0 and 1, the output is passed  
 398 through a sigmoid layer that produces the final predictions.

## 399 **4.4 Experimental set-up**

### 400 *4.4.1 Mesh Definition*

401 To illustrate the advantage of using graph networks, experiments were designed to  
 402 demonstrate the ability to produce forecasts over an irregular mesh. To this end, exper-  
 403 iments were run on an irregular mesh as well as the coarsened regular mesh described  
 404 in Section 4.2 and shown in Figure 2b and Figure 2c. The irregular mesh is refined to  
 405 a higher resolution at the land edges by splitting the base  $1/3^\circ$  mesh if a cell intersects  
 406 a one-cell buffer around land. This buffer is used since near-shore dynamics can be par-  
 407 ticularly complex. By extending high-resolution meshing slightly beyond the immedi-  
 408 ate land-water interface, the model may be better equipped to capture these complex  
 409 dynamics occurring in these more critical regions. The resulting irregular mesh contains  
 410  $1/12^\circ$ ,  $1/6^\circ$  and  $1/3^\circ$  sized cells. To show that the complexities introduced by this ir-  
 411 regular mesh is not a detriment to the model, a separate experiment is conducted by train-  
 412 ing the same model over the regular  $1/3^\circ$  mesh. This should be an easier task than the  
 413 irregular mesh, therefore showing similar performance over either meshes is sufficient to  
 414 demonstrate that the model is resolution-agnostic.

### 415 *4.4.2 Data Partitioning*

416 The Hudson Bay region, including Hudson Strait, James Bay and Foxe Basin, un-  
 417 dergoes a cyclical transformation in its ice cover characterized by complete freezing dur-

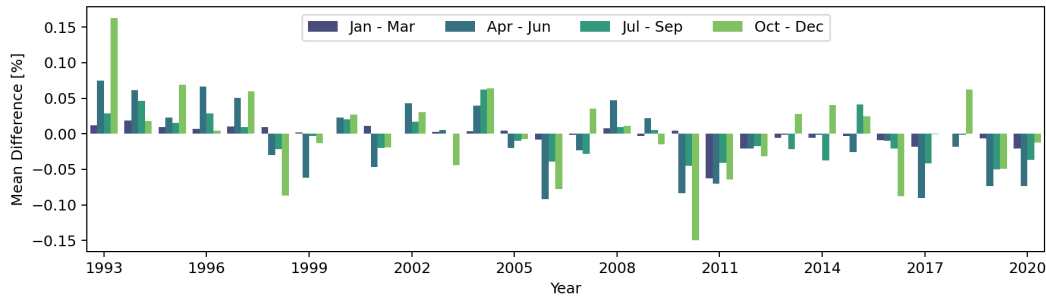


Figure 5: Monthly sea ice concentration anomalies in Hudson Bay from 1993-2020. Highlights periods of higher and lower-than-average sea ice concentrations.

418 ing the winter months and total melt in the summer, with some multi-year ice possible  
 419 in Foxe Basin. This seasonal cycle is subject to considerable inter-annual variability, both  
 420 in terms of the rate at which these processes occur and the timing of these transitions.  
 421 Figure 5 illustrates this variability by showing monthly SIC anomalies between 1993 and  
 422 2020. These anomalies are computed as the mean differences between observed SIC and  
 423 the long-term average concentration for each corresponding month. The data reveals dis-  
 424 tinct periods of anomalous behavior in SIC. Specifically, the years 1993 to 1997 were marked  
 425 by higher-than-average SIC, indicating that during these years, Hudson Bay experienced  
 426 an earlier freeze-up and a delayed break-up season. In contrast, the period from 2010  
 427 to 2012 exhibited anomalously low SIC, characterized by a late onset of freeze-up and  
 428 an earlier melting season. Including data from both these anomalous periods along with  
 429 years that exhibit more typical ice conditions is critical for enhancing model robustness  
 430 in the face of varying environmental conditions. This is particularly important in the con-  
 431 text of climate change, where shifts in temperature and weather patterns could further  
 432 exacerbate the variability in sea ice conditions. The data is therefore partitioned into  
 433 a sequential 20-year, 3-year, 3-year split, wherein data from 1993-2013 is used for train-  
 434 ing, 2013-2016 is used for validation, and 2016-2019 is used for testing. Note however  
 435 that the test period only includes years with normal or lower-than-usual ice conditions.  
 436 Although this bias may not be optimal, lower-than-normal ice conditions may be more  
 437 representative of future ice conditions in the Hudson region (J. Stroeve & Notz, 2018)

438 One model is trained for each month of the year, each denoted as a ‘monthly model’.  
 439 Each monthly model was trained using data from the respective month with a 15-day

440 buffer before and after the beginning and end of the month respectively. For example,  
 441 the April model is trained with input data for each day between March 16 and May 15  
 442 over all training years. A longer buffer of one month was tested but did not lead to sig-  
 443 nificant improvements in model performance. In inference mode, each model is used only  
 444 to produce a forecast with inputs from its respective month. For example, to generate  
 445 90 day forecasts for April, a 90 day forecast is launched for each day between April 1 and  
 446 April 30. Training separate model for each month of the year was done since we expect  
 447 the dynamics that must be learned for one time of the year to be sufficiently different  
 448 from other times of the year such that each model will have greater accuracy by concen-  
 449 trating efforts in learning specific ice dynamics (Asadi et al., 2022). As a secondary ben-  
 450 efit, this also allows training to be carried out more efficiently as each monthly model  
 451 can be trained in parallel.

#### 452 **4.4.3 Input Features**

453 Sea ice concentration data from GLORYS12 serve as the target variable, while at-  
 454 mospheric variables from ERA5, combined with oceanographic variables from GLORYS12,  
 455 are used as input features. Sea ice dynamics are primarily influenced by factors such as  
 456 air and sea temperature (Wang et al., 2019), wind (Stammerjohn et al., 2003), heat fluxes  
 457 (Ivanov et al., 2012), and ocean salinity (Yao et al., 2000), thus we include these vari-  
 458 ables as input features. The 10 chosen input variables are listed in Table 1, along with  
 459 the rationale for their selection. It should be noted that ERA5 hourly variables are re-  
 460 gridded from their original  $0.25^\circ$  grid to match the GLORYS12  $1/12^\circ$  grid, and resam-  
 461 pled to match the GLORYS12 daily temporal resolution. This is achieved through spa-  
 462 tial linear interpolation and aggregation from an hourly to a daily resolution using a sim-  
 463 ple mean. The input sequence length is 10 days and the spatial domain as a grid is  $229 \times$   
 464  $361$ . Since the model operates over the mesh domain rather than the grid domain, the  
 465 dimensionality of the inputs to the encoder as (input steps, number of nodes, input fea-  
 466 tures) is  $10 \times 9,422 \times 10$  for the irregular mesh and  $10 \times 2,425 \times 10$  for the regular  
 467 mesh. The input to the decoder is the context vectors provided by the encoder as well  
 468 as the climatology for each forecast day. The output dimensionality is  $90 \times 9,422 \times 2$   
 469 for the irregular mesh, and  $90 \times 2,425 \times 2$  for the regular mesh.

#### 470 **4.4.4 Baseline Model**

471 As a baseline model with which to compare the model, we use a combination of two  
 472 common statistical baselines: persistence and climatology. Persistence refers to persist-  
 473 ing the most recent sea ice conditions and tends to perform well at very short forecast  
 474 lengths particularly outside of the freezing and melting seasons. Climatology refers to  
 475 the pixel-wise average SIC for each day of the year where the average is taken over the  
 476 historical period of interest. Climatology tends to perform best relative to forecast mod-  
 477 els at longer lead times. For forecasts produced over a seasonal scale, a stronger base-  
 478 line than either persistence and climatology can be derived by combining the two using  
 479 a weighted average with the relative weights varying by lead time, where more weight  
 480 is given to persistence than climatology at short lead times and more weight is given to  
 481 climatology than persistence at long lead times. The form chosen for the baseline model  
 482 is

$$F = (1 - \gamma)P + \gamma C, \quad (6)$$

483 where

$$\gamma(t) = \gamma_0 \times e^{-\lambda t}. \quad (7)$$

484  $\gamma_0$  is set to 1 since we know persistence to be a strong predictor at short lead times, and  
 485  $\lambda$  is optimized by minimizing the mean squared error over the training dataset for each  
 486 month. The resulting weights are shown as a heatmap in Figure 6.

#### 487 **4.4.5 Model Hyperparameter Configurations and Implementation**

488 This study evaluates three distinct models, listed in Table 2. Our primary focus  
 489 is the GraphSIFNet-Att model, which incorporates three TransformerConv spatial con-  
 490 volutions in the GCLSTM block and is trained on the irregular mesh described in Sec-  
 491 tion 4.2 for 35 epochs. That is, in Figure 4b,  $\ast\mathcal{G}$  uses the TransformerConv as the Graph-  
 492 Conv block with  $K = 3$ . For comparison, we examine the GraphSIFNet-Att-Reg model  
 493 which is identical in architecture but trained on the coarsened regular mesh from Sec-  
 494 tion 4.2 for 35 epochs. Additionally, we compare with the GraphSIFNet-GCN model,  
 495 which employs six GCN convolutions within the GCLSTM module, that is, the Graph-  
 496 Conv block is the GCN with  $K = 6$ . GraphSIFNet-GCN is trained over the irregular

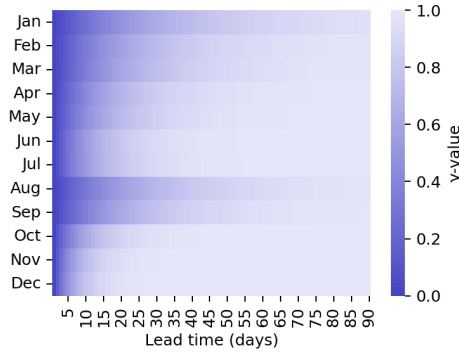


Figure 6: Gamma values for the baseline model (Equation 6) showing the balance between persistence and climatology by the month of the launch date and lead time. Gamma values near 0 favor persistence while values near 1 favor climatology. Less variable ice seasons such as January/February and August/September rely more on persistence for longer lead times.

497 mesh for 45 epochs. Each of these models have the same number of parameters (approx-  
 498 imately 123,000).

499 Each model uses a 10-day input sequence to predict the subsequent 90 days. A hid-  
 500 den dimension size of 32 is used for each of the hidden state and cell state of the encoder  
 501 and decoder LSTMs, as well as in all graph convolutional layers. The GNN used to en-  
 502 code climatology ( $GNN_{enc}$ ) is comprised of a single graph convolution layer, and the out-  
 503 put GNN ( $GNN_{out}$ ) is comprised of 3 stacked convolution layers with leaky ReLU ac-  
 504 tivations. The hidden size, number of spatial convolutions and number of GCLSTM/LSTM  
 505 layers were chosen based on small-scale experiments which aimed to keep the model sim-  
 506 ple yet effective. The optimizer is the Adam optimizer with an initial learning rate of  
 507 0.001 reducing by 10% every 5 epochs. An L2 regularization value of 0.01 is applied to  
 508 the weights reduce the risk of overfitting, and gradient clipping with a value of 1.0 is ap-  
 509 plied to mitigate the risk of gradient explosion due to the extended forecast length. Early  
 510 stopping was used if no improvement in the validation loss was observed for 10 epochs.  
 511 Since the model produces two outputs, a custom loss function was used that combines  
 512 a mean square error (MSE) loss from the continuous SIC prediction and binary cross-  
 513 entropy (BCE) loss from the probabilistic SIP prediction. The BCE loss is scaled by a  
 514 factor of 0.1 and added to the MSE loss before back-propagation. Since losses are cal-

515 culated over a mesh with cells of varying physical sizes, the losses are also scaled by the  
516 size of each cell. This prevents the model from over-valuing correct predictions in areas  
517 of higher spatial resolution. The models are implemented in Pytorch using the pytorch-  
518 geometric (Fey & Lenssen, 2019) package and trained on a single Tesla V100 GPU hosted  
519 by the Digital Research Alliance of Canada. A summary of models tested and training  
520 times is given in Table 2.

## 521 **5 Results**

522 In this section, the GraphSIFNet-Att model is evaluated by comparing its perfor-  
523 mance with the statistical baseline and contrasting with the two other configurations:  
524 GraphSIFNet-Att-Reg and GraphSIFNet-GCN. Using GraphSIFNet-Att, insights from  
525 the attention weights, the results of a variable importance experiment, and an evalua-  
526 tion of its ability to predict break-up and freeze-up dates are also presented.

### 527 **5.1 Baseline Performance**

528 The performance of the baseline statistical model defined by Equation 6 for both  
529 the SIC and SIP forecasting task is shown in Figure 7a and Figure 7b, respectively. These  
530 heatmaps are generated by calculating the spatial average of the root mean squared er-  
531 ror (RMSE) over the domain using only the test years (2016-2019). The errors are grouped  
532 by the month of the launch dates and lead times. For instance, the value in the top right  
533 corner of the error heatmaps (January, 90-day lead time) indicates the mean RMSE for  
534 all 90-day forecasts launched in January, that is, forecasts for dates spanning April 1st  
535 to May 1st. The two clearly visible bands of higher RMSE values correspond to the break-  
536 up and freeze-up seasons, the former normally spanning from the beginning of May to  
537 mid-July and the latter normally spanning from the beginning of November to the end  
538 of December. These seasons are the most difficult to forecast as the timing and pattern  
539 of the break-up and freeze-up vary between years. Conversely, August to beginning of  
540 October are largely ice-free, thus the errors are near zero. In the winter months, that  
541 is, mid-December to the beginning of April, ice is present throughout the Hudson Bay  
542 system though some open water can sporadically be found around shorelines, for exam-  
543 ple due to offshore winds, thus SIC RMSE values during the winter months are small  
544 but not zero.

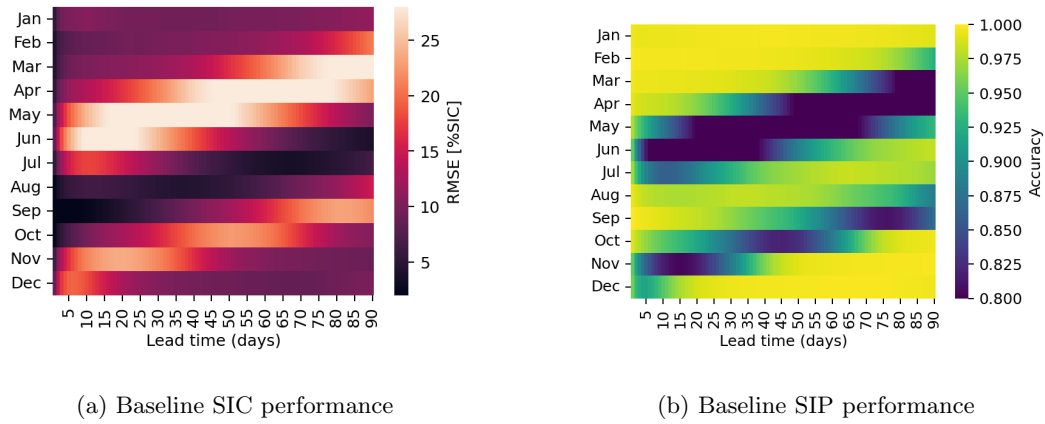


Figure 7: Performance of the baseline statistical model on SIC (a) and SIP (b) over the test years aggregated by the month of the launch date and lead time.

545

## 5.2 GraphSIFNet-Att Performance

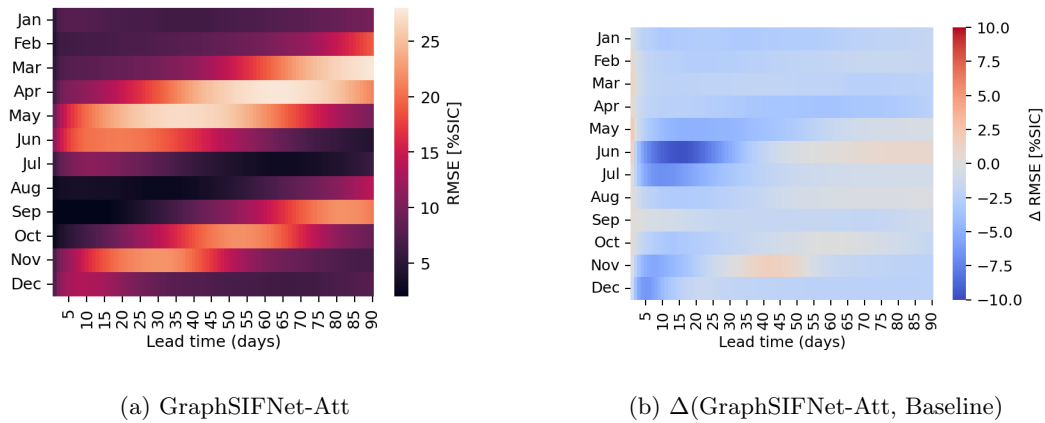


Figure 8: RMSE heatmaps for the SIC forecasting task by month and lead time for the GraphSIFNet-Att model (a), and the RMSE differences between GraphSIFNet-Att and the baseline (b) where negative values (blue) indicate a reduction in model error relative to the baseline.

546

547

548

The performance of GraphSIFNet-Att model and the difference in performance relative to the baseline model is shown in Figure 8 and Figure 9 for SIC and SIP forecasts, respectively. Since persistence and climatology are usually used as baselines separately,

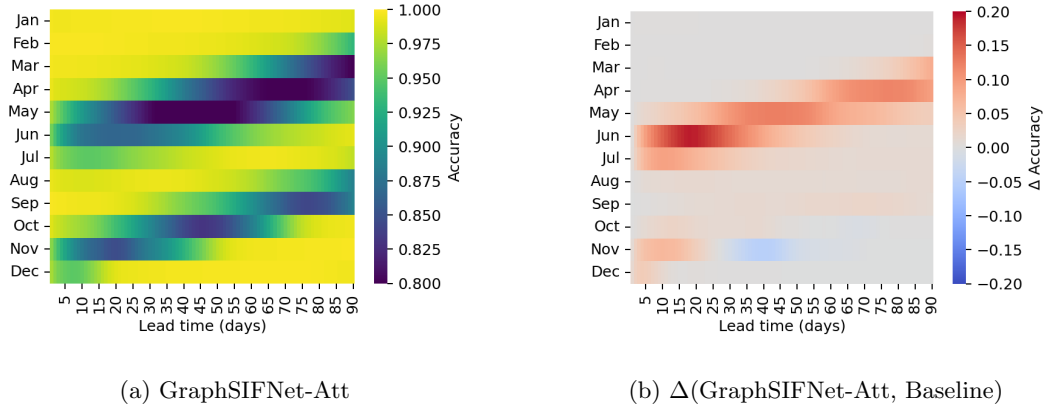


Figure 9: Accuracy heatmaps for the SIP forecasting task by month and lead time for the GraphSIFNet-Att model (a), and the difference between GraphSIFNet-Att and the baseline (b) where positive values (red) in the difference plots indicate an increase in model accuracy relative to the baseline.

549 the difference in performance relative to both are shown in Section Appendix A. Mod-  
 550 els are evaluated against GLORYS12 SIC and SIP on the full-resolution  $1/12^\circ$  GLORYS12  
 551 grid.

552 For the majority of the months and lead times, the GraphSIFNet-Att model ex-  
 553 hibits improvements in SIC forecasts over the baseline, with minor exceptions. The model  
 554 exhibits the largest improvements over the baseline in its short- to medium-term fore-  
 555 casts of the break-up season (lead times 5 to 45 launched in May to July). These show  
 556 up to a 10% improvement over the baseline. At longer timesteps, the improvements over  
 557 the baseline during the break-up period (launched in March and April) are less pronounced,  
 558 hovering around 2-3%. However at these long lead times even small improvements demon-  
 559 strate forecast skill and can provide value to users of the system. During the winter months  
 560 when the region is almost entirely frozen, the model still exhibits a 2-3% improvement  
 561 over the baseline at all lead times. This suggests that the model may be able to better  
 562 capture the effects of off-shore winds mechanically creating open water regions along the  
 563 shoreline. During freeze-up, the model only shows skill over the baseline at short lead  
 564 times from 0 to 25 days. Longer forecasts beyond 25 days perform on par with the base-  
 565 line or only marginally better. Forecasts launched in November with a 30 to 55 day lead

Task	Model	Jan	Feb	Mar	Apr	May	Jun	Jul	Aug	Sep	Oct	Nov	Dec	Avg.
SIC	GraphSIFNet-GCN	0.29	0.19	0.02	0.11	0.67	-0.33	0.18	0.22	0.00	0.11	-0.37	0.40	0.12
	GraphSIFNet-Att-Reg	0.43	0.12	-0.16	0.30	-0.19	-0.71	0.22	0.03	-0.08	1.19	-0.79	0.51	0.07
SIP	GraphSIFNet-GCN	0.00	-0.01	0.05	0.14	-0.54	0.08	-0.06	-0.07	0.37	0.13	-0.38	-0.03	-0.03
	GraphSIFNet-Att-Reg	0.00	-0.03	0.08	-0.22	-0.10	0.25	-0.10	0.02	0.18	-0.21	0.83	-0.15	0.05

Figure 10: Difference in monthly SIC RMSE [%SIC] and SIP [%]accuracy between GraphSIFNet-Att-Reg and GraphSIFNet-GCN relative to GraphSIFNet-Att averaged over all 90 forecast days. Negative RMSE differences and positive accuracy differences indicate better performance on the part of GraphSIFNet-Att relative to the other models.

566 time perform worse than the baseline, indicating difficulty in capturing the final stages  
 567 of ice formation.

568 The SIP accuracy heatmaps in Figure 9 show similar patterns, with increases in  
 569 accuracy of up to 20% from the GraphSIFNet-Att model over the baseline during the  
 570 break-up process, and more modest increases during the freeze-up process. Notably, how-  
 571 ever, GraphSIFNet-Att outperforms quite significantly (> 10%) even at long lead times.  
 572 This indicates that although the model may struggle to forecast the precise SIC at these  
 573 lead times, it still has skill in forecasting the point at which the ice will completely melt  
 574 or break up.

### 575 5.3 Comparison Between Model Configurations

576 Differences in both SIC RMSE and SIP accuracy between the GraphSIFNet model  
 577 configurations, averaged for all timesteps for each month, are shown in Figure 10. GraphSIFNet-  
 578 GCN and GraphSIFNet-Att-Reg demonstrate comparable performance relative to GraphSIFNet-  
 579 Att, with differences being largely insignificant when aggregated across the entire region.  
 580 To better understand the differences in their capabilities, spatial monthly SIC RMSE  
 581 maps for the 15-, 30-, and 60-day lead times for forecasts launched in May and Novem-  
 582 ber are presented in Figure 11. These correspond to parts of the break-up and freeze-  
 583 up periods, respectively. Panels a) and c) show the impact of the convolution operator,  
 584 while panels b) and d) show the impact of the mesh resolution.

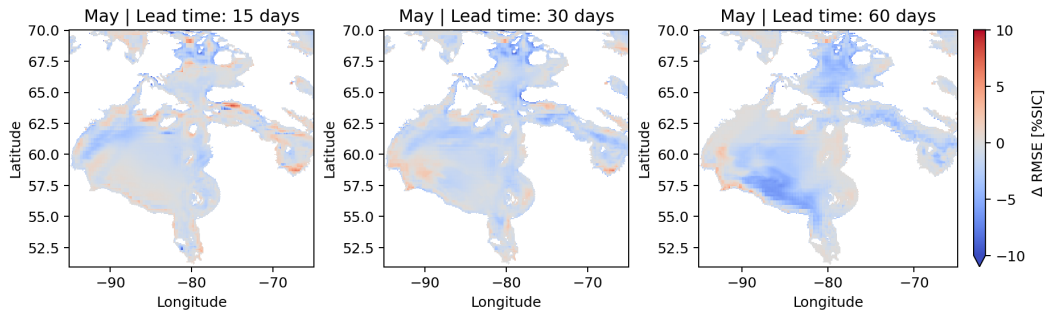
585 Early (15-day) forecasts in the Northwest region of Hudson Bay, launched in May,  
 586 are best captured by GraphSIFNet-Att-Reg. This region is characterized by a latent heat

587 polynya, suggesting that the coarser uniform resolution mesh may aid the model in fore-  
 588 casting the formation and behavior of the polynya. Using a finer resolution mesh in this  
 589 region might cause the model to overemphasize local variations in sea ice concentration  
 590 and thickness, potentially obscuring the broader spatial patterns crucial for accurate polynya  
 591 forecasting. Both GraphSIFNet-GCN and GraphSIFNet-Att-Reg outperform GraphSIFNet-  
 592 Att in the 15- and 30-day forecasts launched in November in Hudson Strait. The freeze-  
 593 up in Hudson Strait is characterized by rapid changes in ice formation and movement  
 594 influenced by strong ocean currents. These conditions create a highly dynamic and chal-  
 595 lenging environment for sea ice prediction. Since all three models exhibit similar perfor-  
 596 mance, the additional interpretability granted by the attention weights in GraphSIFNet-  
 597 Att motivates the use of GraphSIFNet-Att over the others.

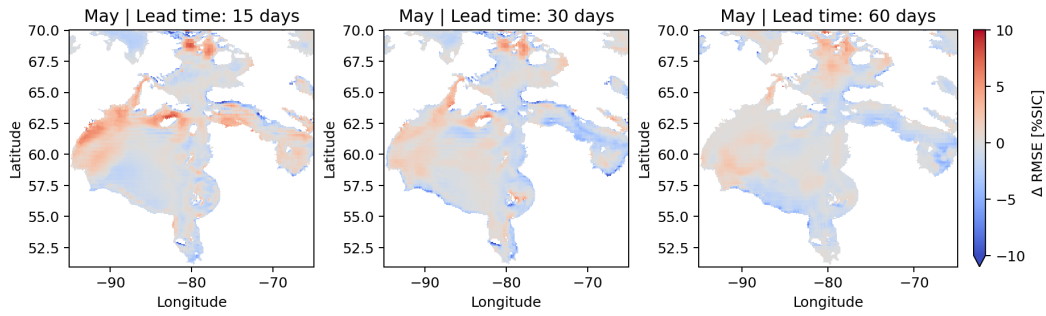
#### 598 **5.4 Attention Maps**

599 The use of transformer convolution in the model enhances its interpretability. By  
 600 examining the attention weights in the encoder’s first layer of graph convolutions, insights  
 601 can be gleaned into how the model encodes the input data. According to Equation 3 and  
 602 Equation 4, each node is assigned attention weights for its neighboring nodes based on  
 603 learned weight matrices in each transformer layer. The softmax function ensures that  
 604 the sum of all attention weights for a given node’s neighbors equals 1. Consequently, the  
 605 node is updated using a weighted average of its neighbors’ features, which are projected  
 606 into a latent space. Due to the large number of edges, visualizing these weights on a sim-  
 607 ple map is challenging. A simpler approach for visualization involves calculating the pri-  
 608 mary direction from which each node is updated. This can be done by summing the at-  
 609 tention weights as vectors ( $\alpha$  values in Equation 3 with the direction of their respective  
 610 edges) for each node. These can be represented by arrows, the magnitude of which is pro-  
 611 portional to the difference in weights. For example, a node with evenly distributed at-  
 612 tention weights among eight neighbors would be represented as a single dot, whereas a  
 613 node with a dominant westward neighbor would have a large arrow pointing westward.  
 614 These arrows can be interpreted as indicating the direction of information flow through  
 615 the graph as the model processes the input maps.

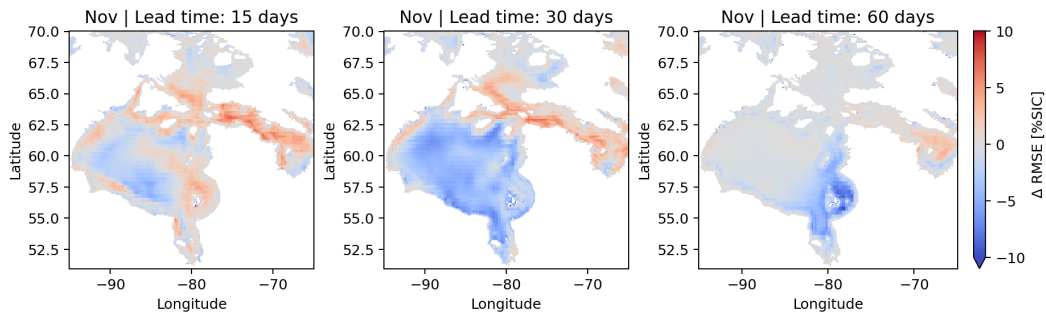
616 Figure 12 provides examples of attention weights of the input gate for a single in-  
 617 put image during both freeze-up (Figure 13a) and melting (Figure 13b) seasons. Although  
 618 the attention mechanism is applied to the hidden and input tensors at each of the LSTM



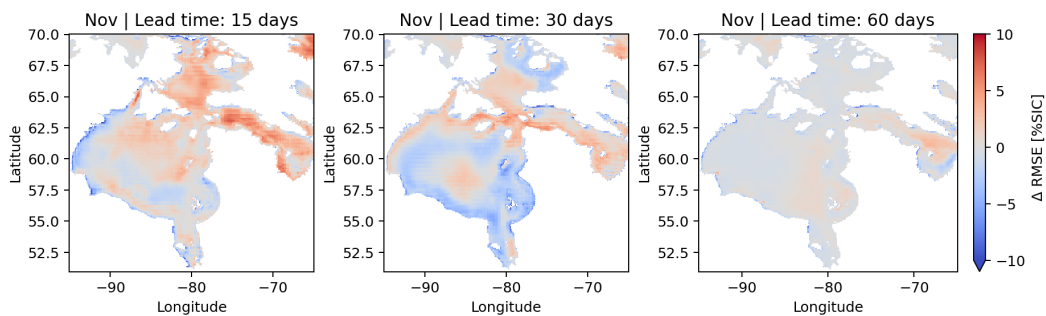
(a) May —  $\Delta$ (GraphSIFNet-Att, GraphSIFNet-GCN)



(b) May —  $\Delta$ (GraphSIFNet-Att, GraphSIFNet-Att-Reg)



(c) November —  $\Delta$ (GraphSIFNet-Att, GraphSIFNet-GCN)



(d) November —  $\Delta$ (GraphSIFNet-Att, GraphSIFNet-Att-Reg)

Figure 11: Comparison of SIC RMSE for GraphSIFNet-Att, GraphSIFNet-Att-Reg, and GraphSIFNet-GCN models at 15-, 30-, and 60-day forecast lead times, initiated in May and November. The figure shows the difference in RMSE between GraphSIFNet-Att and both GraphSIFNet-Att-Reg and GraphSIFNet-GCN. Negative values indicate a reduction in error in the GraphSIFNet-Att relative to the other indicated model.

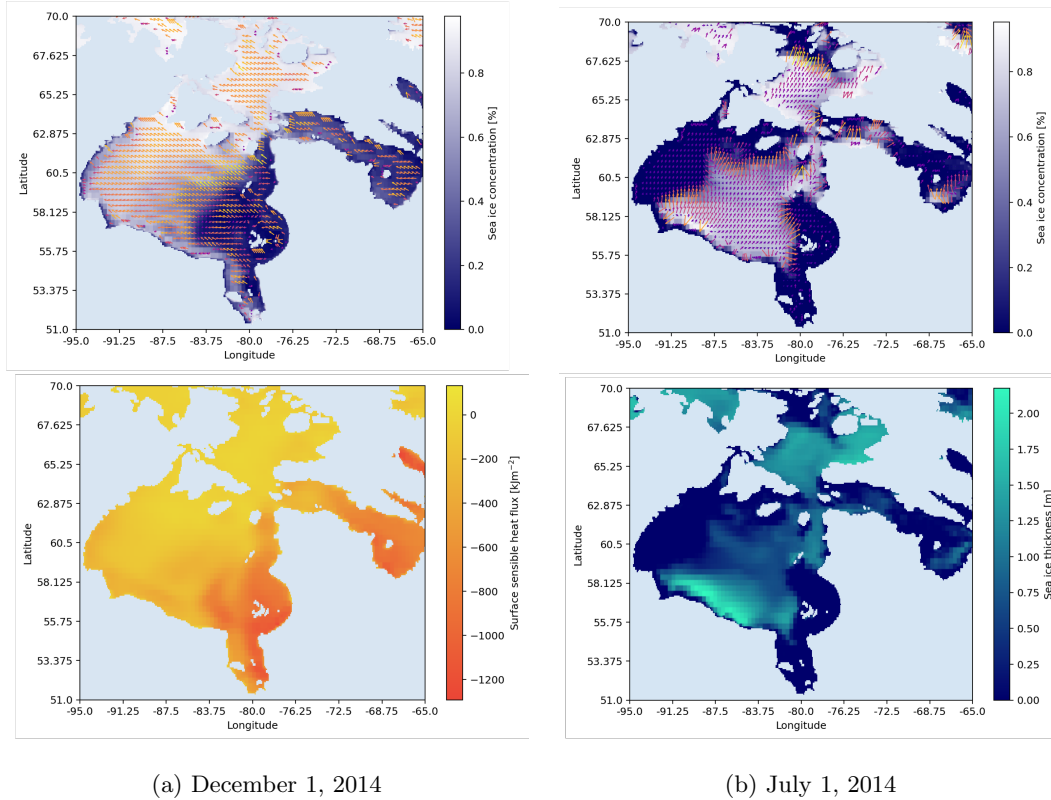


Figure 12: Visualization of attention weights of the input gate applied to the input tensors during the freeze-up (a) and melting (b) seasons overlaid on the sea ice concentration input. Arrows indicate the primary direction and magnitude of information flow based on the learned attention weights. Attention weights at the land interfaces are omitted for clarity. The attention weights appear to be largely influenced by sea ice concentration, but other input variables also influence the weights, for example surface sensible heat flux in (a), and sea ice thickness in (b).

619 gates, it is most informative to visualize the weights that are applied to the inputs since  
 620 the inputs are physically interpretable. Note that attention weights at land interfaces  
 621 are omitted for visual clarity, as they are numerous and the lack of nodes on land means  
 622 the dominant direction is always away from the shore. In the freeze-up condition, the  
 623 model directs information flow generally from the southeast to the northwest. This sug-  
 624 gests that the model learns the importance of understanding the sea ice and atmospheric  
 625 conditions of nodes to the northwest, aligning with the direction of freezing. It is log-  
 626 ical that a node that contains water should know the condition of its 3-hop neighbor to

627 the northwest, as if this neighbor is frozen, it is likely that this node will freeze in the  
 628 near future. Conversely, during the melting season, arrows point towards open water,  
 629 indicating that nodes with icy conditions but with water-containing neighbors should  
 630 consider these neighbors important as they indicate the node is likely to melt soon. No-  
 631 tably, the magnitude of the arrows is larger at the ice edge and nearly zero in the con-  
 632 solidated ice region, which could reflect the localized nature of the break-up process com-  
 633 pared to the more gradual freeze-up. That is, the break-up process is largely confined  
 634 to the ice edge, while freeze-up gradually occurs across the region, as seen by changes  
 635 in sea ice concentration. Nodes in the open water region during the melting season are  
 636 less likely to change and, therefore, do not require attention to specific neighbors. Note  
 637 that although the weights are visualized on the sea ice concentration inputs, they ap-  
 638 ply indiscriminately to all input features. Interestingly, the model appears to prioritize  
 639 sea ice thickness over concentration, evidenced by the larger attention weights where thick-  
 640 ness drops more dramatically than concentration in Figure 13b. This is logical given the  
 641 importance of thickness in determining the rate at which the ice will melt or break up.  
 642 Additionally, the attention weights in the open-water region during the freeze-up condi-  
 643 tion appear to be influenced by surface sensible heat flux, suggesting its significance  
 644 as an input feature.

645 **5.5 Variable Importance**

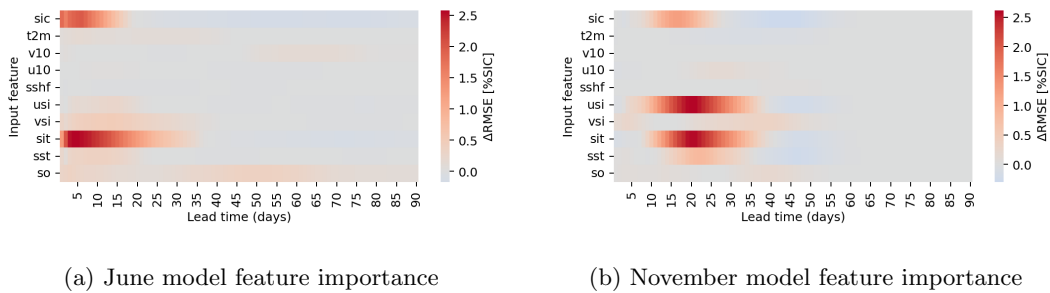


Figure 13: Feature ablation with noise injection for the June and November GraphSIFNet-Att models. Positive values indicate an increase in RMSE when each respective variable is replaced with noise.

646 The models are trained with a number of input variables (refer to Table 1), which  
647 we anticipated the model might utilize to make its predictions. However, these variables  
648 may not contribute equally to the resulting predictions. In this section, we explore the  
649 significance of each feature by feature ablation through omission (Fong & Vedaldi, 2017).  
650 Specifically, we produce forecasts using the trained GraphSIFNet-Att model by substi-  
651 tuting each input variable, one at a time, with white Gaussian noise generated using the  
652 mean and standard deviation of the real inputs. Figure 13 shows the resulting difference  
653 in RMSE when re-generating predictions on the test years using the June and Decem-  
654 ber models when each variable is replaced with noise.

655 During the break-up process (June model), the model largely relies on the input  
656 sea ice concentration and sea ice thickness to make its predictions, but also considers the  
657 ice velocities, sea surface temperature and sea salinity to a smaller degree. Other vari-  
658 ables do not significantly affect the resulting predictions. The model appears to use sea  
659 ice concentrations to inform near-term forecasts (days 0 through 20), and sea ice thick-  
660 ness to inform its medium-term forecasts (days 0 through 35). This makes intuitive sense  
661 as thickness is an indicator of the ice cover’s longevity making it relevant at longer fore-  
662 cast steps, while sea ice concentration is more important for immediate predictions since  
663 lower ice concentrations are normally associated with ice parcels that are already break-  
664 ing up. Note that at forecast steps larger than 35 days, forecasts launched in June are  
665 largely forecasting periods where Hudson Bay is fully open water, thus none of the in-  
666 put features contribute to the resulting forecasts.

667 Similarly, during the freeze-up process, the model relies on sea ice thickness, sea  
668 ice concentration, sea ice velocity and sea surface temperature to make its predictions.  
669 Again, the model largely considers sea ice concentration to make its shorter term fore-  
670 casts (days 10 through 25), while considering ice velocity and thickness for medium-term  
671 forecasts (days 15 through 40). Ice velocity may be indicating areas where ice migrates,  
672 thereby creating space for new ice formation. The difference between the vertical and  
673 horizontal ice velocity component ( $usi$  and  $vs_i$ ) may indicate that they offer redundant  
674 information, thus it is sufficient for the model to consider one of the components. Again,  
675 November forecasts at larger than 40 days are largely forecasting periods of full ice cover,  
676 therefore omitting input features does not impact the scores. It is also worth noting that  
677 in both cases, the model does not appear to consider the variables originating from ERA5.  
678 This could point to a mismatch between ERA5 and GLORYS12, which would be unsur-

679 prising as GLORYS12 uses ERA-Interim as model forcing at the surface. Since the tar-  
680 get variables are derived from GLORYS12, the models therefore prioritize input features  
681 originating from GLORYS12.

682 To illustrate the impact of these variables on the resulting predictions, a sample  
683 GraphSIFNet-Att forecast is shown in Figure 14, along with the same forecast when re-  
684 placing sea ice concentration and sea ice thickness (SIT) with noise as described above.  
685 Replacing either SIC or SIT with noise does not significantly affect the 1-day forecast,  
686 suggesting the model uses persistence as a heuristic at very short lead times. Beyond the  
687 10-day forecast, predictions are affected by the noise injections, with the model forecast-  
688 ing a quicker melt when sea ice thickness is replaced with noise, consistent with the theo-  
689 ry that thickness is used as a signal of ice longevity. When SIC is replaced with noise,  
690 the model persists more of the ice in the 20-day forecast, suggesting that SIC is also im-  
691 portant for ice integrity.

692 Although this technique offers some insight into feature importance, it should be  
693 noted that since the models are not re-trained, the observed changes in performance due  
694 to feature omission may not perfectly reflect the true importance of each feature. This  
695 is because the model has been optimized to make predictions based on the full set of fea-  
696 tures, therefore the omission of any one feature changes the input space in a way that  
697 the model was not specifically trained to handle. Moreover, the interdependencies be-  
698 tween features are not accounted for in this single-feature ablation approach. Variables  
699 in the dataset may interact in complex, non-linear ways that are not captured by exam-  
700 ining each variable in isolation. Despite these limitations, this feature ablation technique  
701 provides useful insights into the relative importance of the different input features used  
702 in these particular trained models (Fong & Vedaldi, 2017). Since we know which features  
703 the models are using, we know which input variables should be more closely monitored.

## 704 **5.6 Estimating Break-up and Freeze-up Dates**

705 A potential use-case for sea ice prediction in Hudson Bay is the estimation of break-  
706 up and freeze-up dates in key locations, as these dates have significant implications for  
707 maritime navigation and local communities. We evaluate the GraphSIFNet-Att model’s  
708 performance in estimating the freeze-up date at three key ports in Hudson Bay: the ports  
709 of Churchill, Quaqtaq and Inukjuak. The port of Churchill is mostly used to export grain

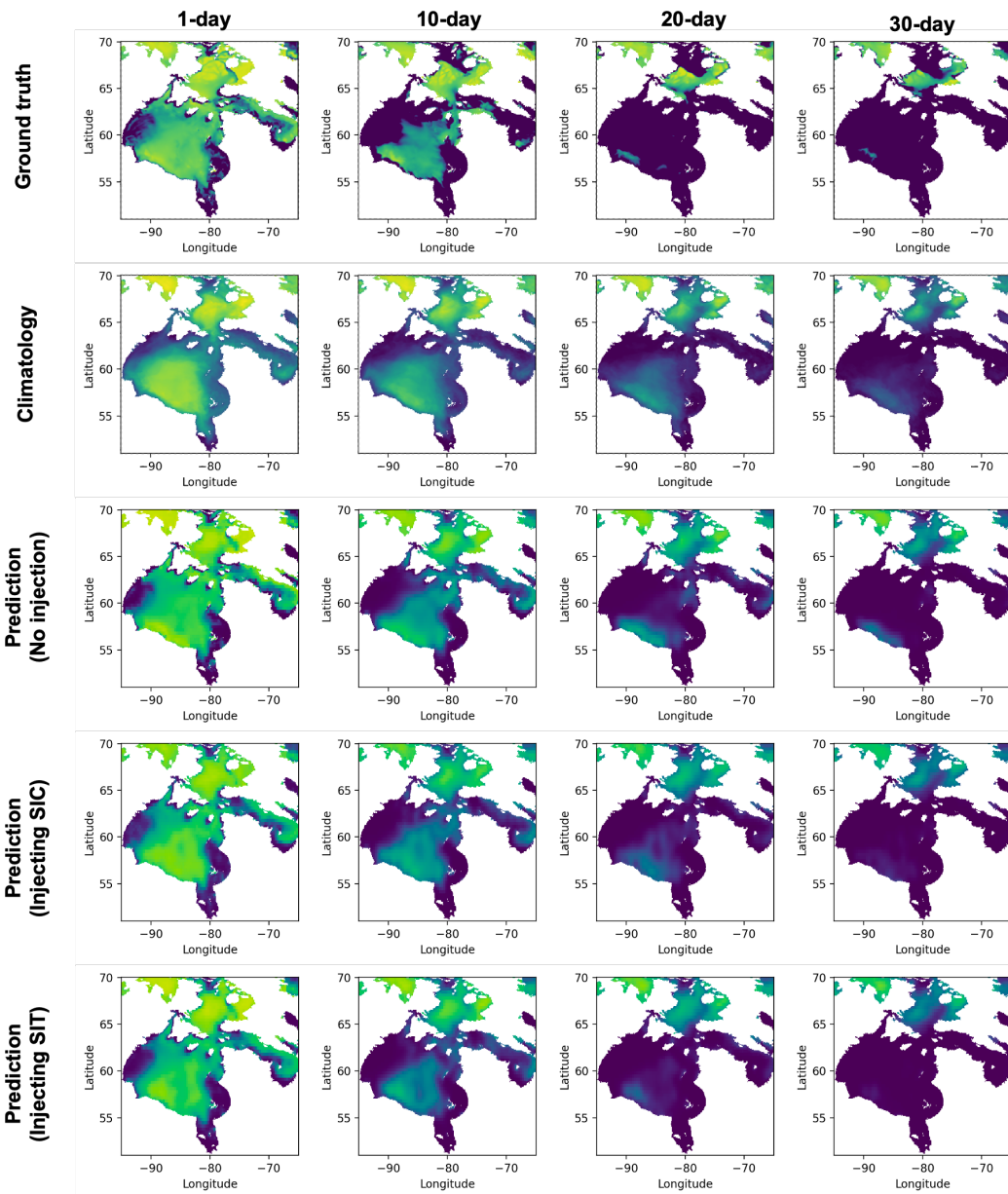
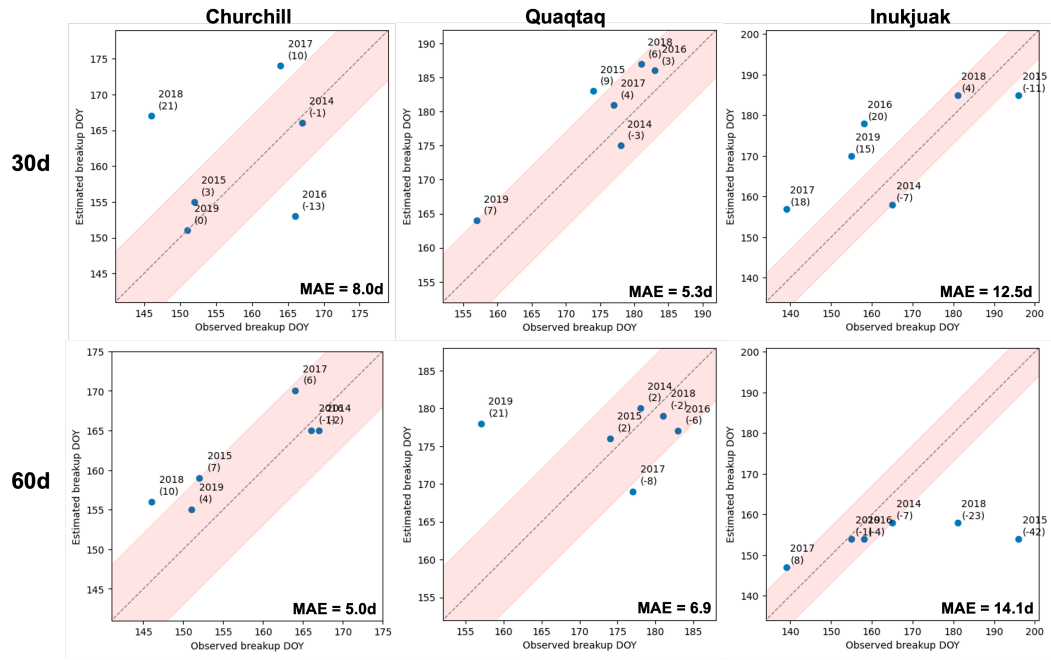


Figure 14: Sample 1-, 10-, 20-, and 30-day forecasts from GraphSIFNet-Att launched on June 15, 2014. The climatology for each forecast day is shown for reference, and the results of running inference after replacing sea ice concentration (SIC) and sea ice thickness (SIT) with noise is shown.

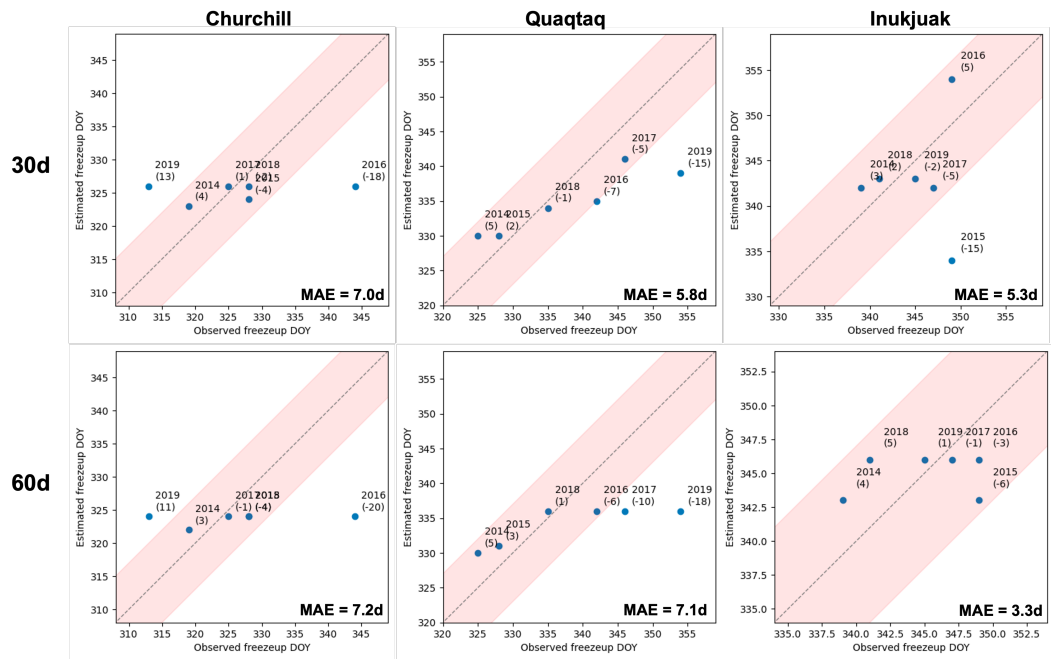
710 while the ports of Quaqtaq and Inukjuak are regularly used for community resupply. These  
711 three ports were chosen as their locations are representative of the varying sea ice con-  
712 ditions found in the Hudson Bay region. In this study, the validation and test year (2014  
713 to 2019) serve as the period for assessing the predicted break-up and freeze-up dates. These  
714 dates are determined using the same criteria as the previous study, which follows the def-  
715 inition given by the Canadian Ice Service (CIS). That is, the freeze-up date at a given  
716 site is defined as the initial day when open water persists for 15 consecutive days, with  
717 open water being defined as a SIC of less than 15%. Conversely, the break-up date is de-  
718 fined as first day at which SIC exceeds 15% for 15 consecutive days. The 30-day and 60-  
719 day predicted break-up and freeze-up dates are determined using the same criteria, but  
720 with open water and ice conditions being defined as a sea ice presence probability less  
721 than and greater than 50%, respectively. For each port, we take the mean pixel value  
722 of a  $3 \times 3$  window around the nearest pixel to the port locations.

723 Figure 15 displays the predicted dates of freeze-up/breakup at the three ports with  
724 30 and 60 days of lead time compared to the actual observed dates for the validation and  
725 test years along with the mean absolute error. Predicted dates falling within 7 days of  
726 the observed dates are considered correct, visualized by the pink shaded area. This def-  
727 inition of a correct forecast is in line with a previous study (Asadi et al., 2022). The 30-  
728 day forecasted break-up and freeze-up dates for Churchill are noticeably inferior to the  
729 other two ports, likely due to challenges presented by the latent heat polynya in the North-  
730 west of Hudson Bay. The uniform forecasts of freeze-up dates at Churchill can be inter-  
731 preted as an admission that the model does not have skill here and resorts to forecast-  
732 ing the same mean day every year. Break-up predictions at Inukjuak also pose a chal-  
733 lenge for the model, likely due to freshwater inflows from the James Bay area affecting  
734 the timing and rate of melt. Quaqtaq sees the most successful predictions, with all freeze-  
735 up dates falling within 7 days of the observed date.

736 In Figure 16, the break-up and freeze-up accuracies are shown spatially for the en-  
737 tire region. These accuracies are calculated as the proportion of years with predicted break-  
738 up or freeze-up dates within 7 days of the observed date. These are compared to pre-  
739 dictions made using the climate normals. The model performs equally or better than cli-  
740 matology for most of the region in predicting break-up dates at both 30-days and 60-  
741 days of lead time. However, there is a strong pattern in the freeze-up maps where the  
742 model performs worse than climatology in the western half of the bay but still outper-



(a) Break-up date estimates



(b) Freeze-up date estimates

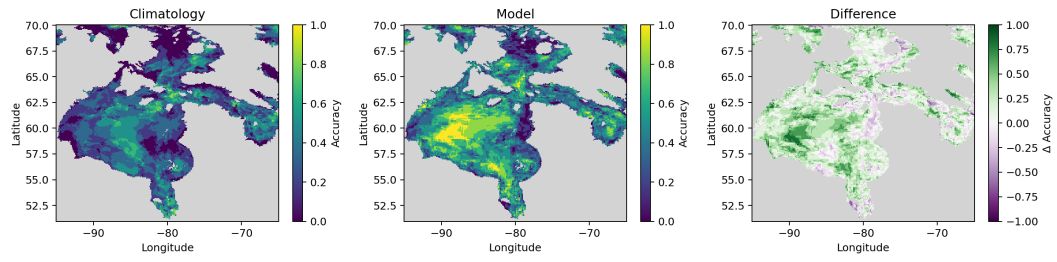
Figure 15: Break-up and freeze-up dates predicted by GraphSIFNet-Att at Churchill, Inukjuak, and Quaqtq ports for lead times of 30 and 60 days for the years 2014 to 2019 compared to the observed dates from GLORYS12. The pink shaded area represents a 7-day buffer around a perfect forecast. Samples which fall within this buffer are deemed correct forecasts. The annotated numbers in parentheses are the error for each year.

743 forms climatology in the eastern half and in Hudson Strait. This is unsurprising as Hud-  
744 son Bay begins its freeze-up process in the northwest corner of the bay, thus the onset  
745 of that initial freezing is difficult to predict. Once the bay has begun freezing over, the  
746 model can better predict the timing of the rest of the bay. Although we might expect  
747 the model to use atmospheric conditions such as temperature to predict the onset of freeze-  
748 up, the model only has access those atmospheric conditions 30 or 60 days prior to the  
749 forecast date. There may not be a strong enough signal in those initial conditions to al-  
750 low the model to accurately predict how quickly the temperatures will drop.

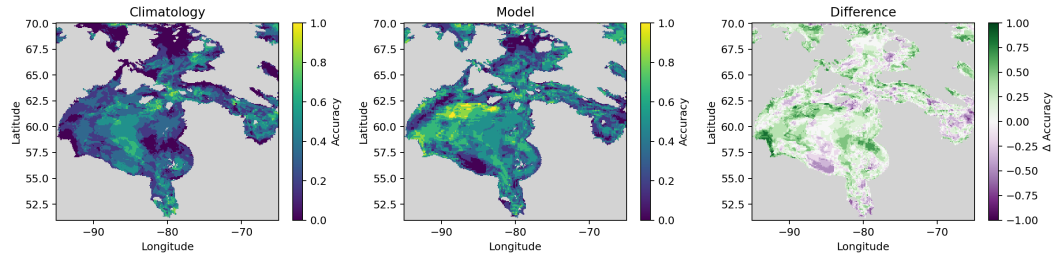
## 751 **6 Conclusion**

752 The study presented in this paper demonstrated the effectiveness of using a GNN-  
753 based spatiotemporal forecasting model for predicting daily sea ice concentration and  
754 sea ice presence in Hudson Bay over a 90-day time horizon. To demonstrate the ability  
755 of GNNs to handle spatially irregular meshes, models were trained on both a uniform  
756 regular mesh and an irregular mesh with higher resolution near shorelines. The proposed  
757 model uses an attention-based transformer spatial convolution to learn spatial features  
758 from the input, which was shown to have similar performance compared to the more ba-  
759 sic graph convolutional network. The attention-based convolution however has the ad-  
760 ditional benefit of increasing the model’s interpretability, motivating its use.

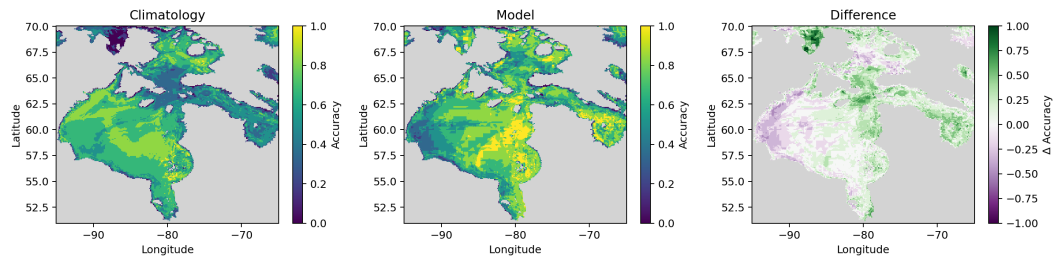
761 Results from this study highlighted the model’s skill in predicting sea ice dynam-  
762 ics, with particular success noted in short- to medium-term forecasts during the break-  
763 up season when compared to a linear combination of persistence and climatology as a  
764 statistical baseline. The model performed as well or better on the irregular mesh as on  
765 the regular mesh, with the exception of some difficulty capturing the initial freeze-up in  
766 the Northwest region of Hudson Bay as well as the polynya formation at longer lead times.  
767 This suggests that improvements could be made in refining the model’s sensitivity to com-  
768 plex spatial features associated with irregular meshes, particularly in areas where ice dy-  
769 namics are highly variable. This could involve more sophisticated positional and spatial  
770 encoding, perhaps by projecting the positional, cell size, distance and angle encodings  
771 into higher dimensional latent space. The model showed similar overall performance be-  
772 tween the model using the transformer convolution and the GCN within the GCLSTM  
773 module, with some differences in performance in certain regions such as Hudson Strait.



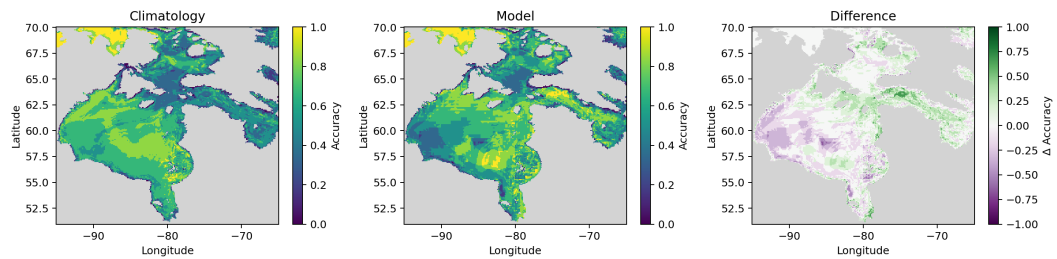
(a) 30-day break-up date estimate map



(b) 60-day break-up date estimate map



(c) 30-day freeze-up date estimate map



(d) 60-day freeze-up date estimate map

Figure 16: Break-up and freeze-up date estimate maps from the climatological baseline (a), GraphSIFNet-Att model predictions (b), and the difference between the two (c). Positive values in the difference plots indicate an increase in accuracy from the model relative to the baseline, where accuracy is defined as the proportion of predictions falling within 7 days of the observed date for the years 2014 to 2019.

774 This suggested potential overfitting in the model using the spatial transformer convo-  
775 lution.

776 The attention mechanism within the transformer convolution offered interpretabil-  
777 ity by highlighting the primary direction and magnitude of information flow in the en-  
778 coder, which aligned with known physical processes such as the direction of freezing and  
779 melting. A feature ablation experiment indicated the trained model’s reliance on sea ice  
780 concentration, thickness and velocities to inform its predictions. Other variables did not  
781 contribute significantly to the resulting forecasts, which could explain the model’s poor  
782 performance in forecasting the Kivalliq latent heat polynya. A evaluation of the model’s  
783 ability to predict freeze-up and break-up dates was conducted, revealing the model’s lim-  
784 ited ability to forecast the onset of freeze-up in Hudson Bay, as well as the onset of break-  
785 up in the Northwest region which is influenced by the polynya. The model however still  
786 showed skill over the statistical baseline in these tasks.

787 Several potential avenues for future work exist. In a GNN, each node is processed  
788 as a separate sample by the network. This has two major implications. First, one input  
789 image  $X \in \mathbb{R}^{W \times H \times C}$  does not necessarily need to be processed fully at once, instead,  
790 nodes could also be sampled in batches sequentially until the full sample has been pro-  
791 cessed. This would be helpful in the case where the region is large and modelling it in  
792 its entirety would be infeasible due to memory constraints. Second, since each node has  
793 its own hidden and cell states, cells can be combined by averaging the states or split by  
794 duplicating the states. This means that the underlying mesh could be dynamic in time,  
795 evolving as the underlying data changes (e.g. as the ice conditions evolves). For exam-  
796 ple, one could define a dynamic mesh which has a higher resolution at the ice edge where  
797 the ice conditions are known to be more dynamic. As the ice conditions evolve, so too  
798 would the underlying mesh. The advantages are two-fold. First, it allows for a reduc-  
799 tion in data volume with minimal information loss, contrary to the static mesh used in  
800 this work which has information loss where the data has high spatial variance. Second,  
801 the dynamic mesh could help the model learn more sophisticated dynamics and is more  
802 consistent with physical simulation software. This idea was explored in (Pfaff et al., 2020).  
803 Another avenue for future work could be a deeper investigation of the adjacency matrix.  
804 In this study, edges were placed between any two directly spatially adjacent cells. How-  
805 ever, edges could also be placed between distant cells thereby widening the receptive field  
806 without adding convolutions. This could be investigated by transforming the adjacency

807 matrix into a learnable matrix optimized during training. Furthermore, node sampling  
 808 strategies could also be used to reduce training time. Specifically, adaptive sampling tech-  
 809 niques could be employed where nodes in dynamic regions, such as the ice edges known  
 810 for their fluctuating conditions, are sampled with higher frequency compared to the more  
 811 static areas. Incorporating long-term weather forecasts from third party sources such as  
 812 the Canadian Global Ice Ocean Prediction System (GIOPS) could also be beneficial, par-  
 813 ticularly in forecasting freeze-up. Lastly, multi-resolution modelling either through an  
 814 ensemble of models operating over meshes of different resolution or using multiple meshes  
 815 of varying resolutions within a single model could be explored. This may help the model  
 816 better capture both large-scale and small-scale phenomena.

## 817 Appendix A Additional RMSE Heatmaps

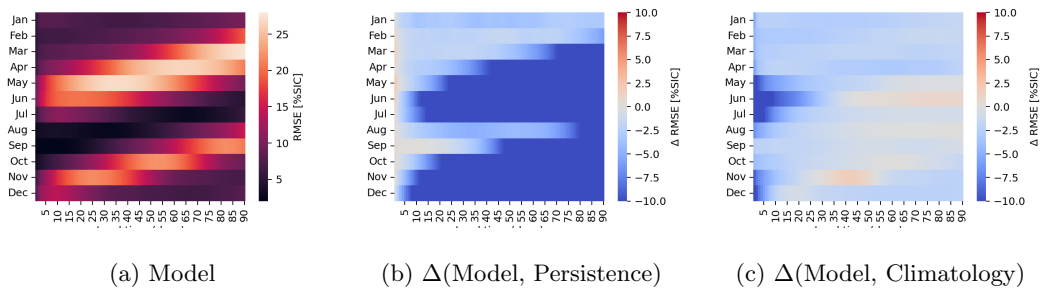


Figure A1: RMSE heatmaps for the SIC forecasting task by month and lead time for the GraphSIFNet-Att model (a), and the RMSE differences between GraphSIFNet-Att and persistence (b) and climatology (c) where negative values (blue) indicate a reduction in model error relative to the baseline.

## 818 Data Availability Statement

819 ERA5 atmospheric reanalysis data (Hersbach et al., 2020) are available at [https://](https://doi.org/10.24381/cds.adbb2d47)  
 820 [doi.org/10.24381/cds.adbb2d47](https://doi.org/10.24381/cds.adbb2d47), and GLORYS12 ocean reanalysis data (Jean-Michel  
 821 et al., 2021) are available at <https://doi.org/10.48670/moi-00021>.

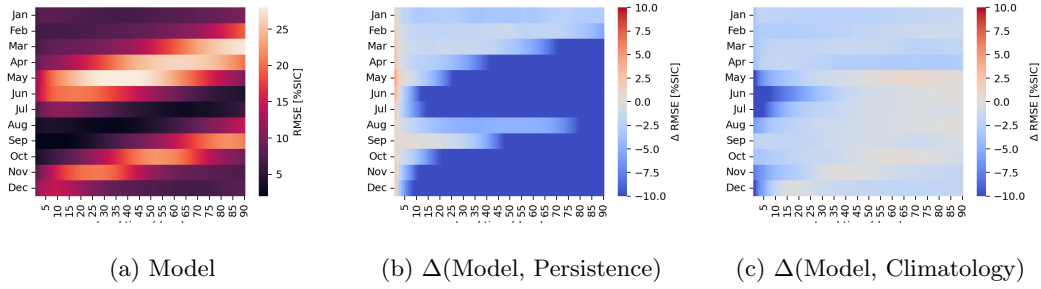


Figure A2: RMSE heatmaps for the SIC forecasting task by month and lead time for the GraphSIFNet-Att-Reg model (a), and the RMSE differences between GraphSIFNet-Att-Reg and persistence (b) and climatology (c) where negative values (blue) indicate a reduction in model error relative to the baseline.

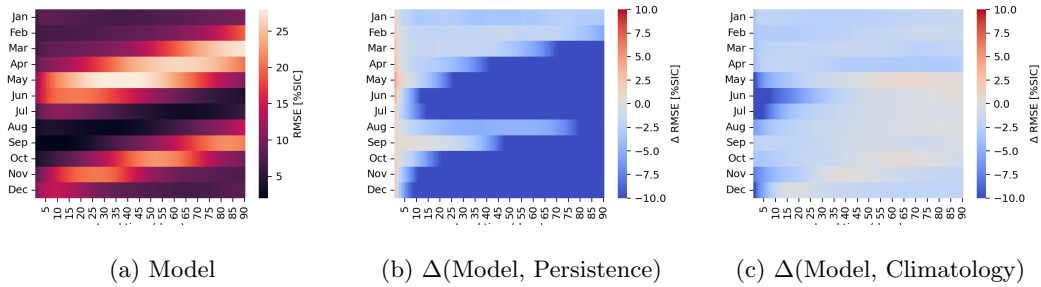


Figure A3: RMSE heatmaps for the SIC forecasting task by month and lead time for the GraphSIFNet-Att-Reg model (a), and the RMSE differences between GraphSIFNet-GCN and persistence (b) and climatology (c) where negative values (blue) indicate a reduction in model error relative to the baseline.

822 **Acknowledgments**

823 The authors would like to acknowledge funding from the National Research Council Canada  
 824 through the AI4Logistics and Ocean programs and computing resources provided by the  
 825 Digital Research Alliance of Canada.

826 **References**

827 Andersson, T. R., Hosking, J. S., Pérez-Ortiz, M., Paige, B., Elliott, A., Rus-  
 828 sell, C., ... Shuckburgh, E. (2021, August). Seasonal Arctic sea ice fore-

- 829 casting with probabilistic deep learning. *Nature Communications*, 12(1),  
 830 5124. Retrieved 2022-09-28, from [https://www.nature.com/articles/](https://www.nature.com/articles/s41467-021-25257-4)  
 831 [s41467-021-25257-4](https://www.nature.com/articles/s41467-021-25257-4) (Number: 1 Publisher: Nature Publishing Group) doi:  
 832 10.1038/s41467-021-25257-4
- 833 Anselin, L. (1988). A Typology of Spatial Econometric Models. In L. Anselin (Ed.),  
 834 *Spatial Econometrics: Methods and Models* (pp. 32–40). Dordrecht: Springer  
 835 Netherlands. Retrieved 2023-11-16, from [https://doi.org/10.1007/978-94-](https://doi.org/10.1007/978-94-015-7799-1_4)  
 836 [015-7799-1\\_4](https://doi.org/10.1007/978-94-015-7799-1_4) doi: 10.1007/978-94-015-7799-1\_4
- 837 Asadi, N., Lamontagne, P., King, M., Richard, M., & Scott, K. A. (2022,  
 838 September). Probabilistic spatiotemporal seasonal sea ice presence fore-  
 839 casting using sequence-to-sequence learning and ERA5 data in the Hud-  
 840 son Bay region. *The Cryosphere*, 16(9), 3753–3773. Retrieved 2022-10-  
 841 16, from <https://tc.copernicus.org/articles/16/3753/2022/> doi:  
 842 10.5194/tc-16-3753-2022
- 843 Ba, J. L., Kiros, J. R., & Hinton, G. E. (2016, July). *Layer Normalization*.  
 844 arXiv. Retrieved 2023-09-19, from <http://arxiv.org/abs/1607.06450>  
 845 (arXiv:1607.06450 [cs, stat])
- 846 Cavalieri, D. J., & Parkinson, C. L. (2012, August). Arctic sea ice variability and  
 847 trends, 1979–2010. *The Cryosphere*, 6(4), 881–889. Retrieved 2022-04-18, from  
 848 <https://tc.copernicus.org/articles/6/881/2012/> (Publisher: Coperni-  
 849 cus GmbH) doi: 10.5194/tc-6-881-2012
- 850 Chi, J., & Kim, H.-c. (2017, December). Prediction of Arctic Sea Ice Concentra-  
 851 tion Using a Fully Data Driven Deep Neural Network. *Remote Sensing*, 9(12),  
 852 1305. Retrieved 2023-07-28, from [https://www.mdpi.com/2072-4292/9/12/](https://www.mdpi.com/2072-4292/9/12/1305)  
 853 [1305](https://www.mdpi.com/2072-4292/9/12/1305) (Number: 12 Publisher: Multidisciplinary Digital Publishing Institute)  
 854 doi: 10.3390/rs9121305
- 855 Dee, D. P., Uppala, S. M., Simmons, A. J., Berrisford, P., Poli, P., Kobayashi, S.,  
 856 ... Vitart, F. (2011). The ERA-Interim reanalysis: configuration and per-  
 857 formance of the data assimilation system. *Quarterly Journal of the Royal*  
 858 *Meteorological Society*, 137(656), 553–597. Retrieved 2023-06-01, from  
 859 <https://onlinelibrary.wiley.com/doi/abs/10.1002/qj.828> (eprint:  
 860 <https://onlinelibrary.wiley.com/doi/pdf/10.1002/qj.828>) doi: 10.1002/qj.828
- 861 Fey, M., & Lenssen, J. E. (2019, April). *Fast Graph Representation Learn-*

- 862 *ing with PyTorch Geometric.* arXiv. Retrieved 2022-11-27, from  
863 <http://arxiv.org/abs/1903.02428> (arXiv:1903.02428 [cs, stat]) doi:  
864 10.48550/arXiv.1903.02428
- 865 Fong, R. C., & Vedaldi, A. (2017, October). Interpretable Explanations of Black  
866 Boxes by Meaningful Perturbation. In *2017 IEEE International Conference on*  
867 *Computer Vision (ICCV)* (pp. 3449–3457). Venice: IEEE. Retrieved 2023-11-  
868 09, from <http://ieeexplore.ieee.org/document/8237633/> doi: 10.1109/  
869 ICCV.2017.371
- 870 Gers, F., Schraudolph, N., & Schmidhuber, J. (2002, January). Learning Precise  
871 Timing with LSTM Recurrent Networks. *Journal of Machine Learning Re-*  
872 *search*, 3, 115–143. doi: 10.1162/153244303768966139
- 873 Hamilton, W., Ying, Z., & Leskovec, J. (2017). Inductive Representation  
874 Learning on Large Graphs. In *Advances in Neural Information Process-*  
875 *ing Systems* (Vol. 30). Curran Associates, Inc. Retrieved 2023-11-09,  
876 from [https://proceedings.neurips.cc/paper\\_files/paper/2017/hash/](https://proceedings.neurips.cc/paper_files/paper/2017/hash/5dd9db5e033da9c6fb5ba83c7a7e9bea9-Abstract.html)  
877 [5dd9db5e033da9c6fb5ba83c7a7e9bea9-Abstract.html](https://proceedings.neurips.cc/paper_files/paper/2017/hash/5dd9db5e033da9c6fb5ba83c7a7e9bea9-Abstract.html)
- 878 He, K., Zhang, X., Ren, S., & Sun, J. (2016, June). Deep Residual Learning for Im-  
879 age Recognition. In *2016 IEEE Conference on Computer Vision and Pattern*  
880 *Recognition (CVPR)* (pp. 770–778). Las Vegas, NV, USA: IEEE. Retrieved  
881 2023-11-09, from <http://ieeexplore.ieee.org/document/7780459/> doi: 10  
882 .1109/CVPR.2016.90
- 883 He, M., Wei, Z., & Wen, J.-R. (n.d.). Convolutional Neural Networks on Graphs  
884 with Chebyshev Approximation, Revisited.
- 885 Hersbach, H., Bell, B., Berrisford, P., Hirahara, S., Horányi, A., Muñoz Sabater,  
886 J., ... Thépaut, J. N. (2020, July). The ERA5 global reanalysis. *Quarterly*  
887 *Journal of the Royal Meteorological Society*, 146(730), 1999–2049. Retrieved  
888 2022-09-28, from <https://onlinelibrary.wiley.com/doi/10.1002/qj.3803>  
889 doi: 10.1002/qj.3803
- 890 Ivanov, V. V., Alexeev, V. A., Repina, I., Koldunov, N. V., & Smirnov, A. (2012,  
891 August). Tracing Atlantic Water Signature in the Arctic Sea Ice Cover East  
892 of Svalbard. *Advances in Meteorology*, 2012, e201818. Retrieved 2023-09-14,  
893 from <https://www.hindawi.com/journals/amete/2012/201818/> (Publisher:  
894 Hindawi) doi: 10.1155/2012/201818

- 895 Jean-Michel, L., Eric, G., Romain, B.-B., Gilles, G., Angélique, M., Marie, D.,  
 896 ... Pierre-Yves, L. T. (2021). The Copernicus Global 1/12° Oceanic and  
 897 Sea Ice GLORYS12 Reanalysis. *Frontiers in Earth Science*, 9. Retrieved  
 898 2022-09-28, from [https://www.frontiersin.org/articles/10.3389/](https://www.frontiersin.org/articles/10.3389/feart.2021.698876)  
 899 [feart.2021.698876](https://www.frontiersin.org/articles/10.3389/feart.2021.698876)
- 900 Joshi, A., Deshmukh, P. K., & Lohokare, J. (2022, June). Comparative analysis of  
 901 Vanilla LSTM and Peephole LSTM for stock market price prediction. In *2022*  
 902 *International Conference on Computing, Communication, Security and Intelli-*  
 903 *gent Systems (IC3SIS)* (pp. 1–6). doi: 10.1109/IC3SIS54991.2022.9885528
- 904 Kalman, R. E. (1960, March). A New Approach to Linear Filtering and Prediction  
 905 Problems. *Journal of Basic Engineering*, 82(1), 35–45. Retrieved 2023-11-16,  
 906 from <https://doi.org/10.1115/1.3662552> doi: 10.1115/1.3662552
- 907 Keisler, R. (2022, February). *Forecasting Global Weather with Graph Neural Net-*  
 908 *works*. arXiv. Retrieved 2022-07-05, from <http://arxiv.org/abs/2202.07575>  
 909 (Number: arXiv:2202.07575 arXiv:2202.07575 [physics])
- 910 Kim, J., Kim, K., Cho, J., Kang, Y. Q., Yoon, H.-J., & Lee, Y.-W. (2019, Jan-  
 911 uary). Satellite-Based Prediction of Arctic Sea Ice Concentration Using a  
 912 Deep Neural Network with Multi-Model Ensemble. *Remote Sensing*, 11(1),  
 913 19. Retrieved 2023-07-28, from <https://www.mdpi.com/2072-4292/11/1/19>  
 914 (Number: 1 Publisher: Multidisciplinary Digital Publishing Institute) doi:  
 915 10.3390/rs11010019
- 916 Kipf, T. N., & Welling, M. (2017, February). *Semi-Supervised Classification with*  
 917 *Graph Convolutional Networks*. arXiv. Retrieved 2022-11-27, from [http://](http://arxiv.org/abs/1609.02907)  
 918 [arxiv.org/abs/1609.02907](http://arxiv.org/abs/1609.02907) (arXiv:1609.02907 [cs, stat]) doi: 10.48550/arXiv  
 919 .1609.02907
- 920 Lam, R., Sanchez-Gonzalez, A., Willson, M., Wirnsberger, P., Fortunato, M.,  
 921 Pritzel, A., ... Battaglia, P. (2022, December). *GraphCast: Learning skill-*  
 922 *ful medium-range global weather forecasting*. arXiv. Retrieved 2023-01-30, from  
 923 <http://arxiv.org/abs/2212.12794> (arXiv:2212.12794 [physics])
- 924 Liu, Y., Bogaardt, L., Attema, J., & Hazeleger, W. (2021, March). Extended Range  
 925 Arctic Sea Ice Forecast with Convolutional Long-Short Term Memory Net-  
 926 works. *Monthly Weather Review*, 149. doi: 10.1175/MWR-D-20-0113.1
- 927 Madec, G. (n.d.). NEMO ocean engine.

- 928 Meier, W. N., Hovelsrud, G. K., van Oort, B. E., Key, J. R., Kovacs, K. M.,  
929 Michel, C., ... Reist, J. D. (2014). Arctic sea ice in transformation: A  
930 review of recent observed changes and impacts on biology and human ac-  
931 tivity. *Reviews of Geophysics*, 52(3), 185–217. Retrieved 2022-04-18, from  
932 <https://onlinelibrary.wiley.com/doi/abs/10.1002/2013RG000431>  
933 (\_eprint: <https://onlinelibrary.wiley.com/doi/pdf/10.1002/2013RG000431>)  
934 doi: 10.1002/2013RG000431
- 935 Moon, T. A., Overeem, I., Druckenmiller, M., Holland, M., Huntington, H.,  
936 Kling, G., ... Wong, G. (2019). The Expanding Footprint of Rapid Arc-  
937 tic Change. *Earth's Future*, 7(3), 212–218. Retrieved 2022-04-18, from  
938 <https://onlinelibrary.wiley.com/doi/abs/10.1029/2018EF001088>  
939 (\_eprint: <https://onlinelibrary.wiley.com/doi/pdf/10.1029/2018EF001088>)  
940 doi: 10.1029/2018EF001088
- 941 Mudryk, L., Dawson, J., Howell, S., Derksen, C., Zagon, T., & Brady, M. (2021,  
942 August). Impact of 1, 2 and 4 °C of global warming on ship naviga-  
943 tion in the Canadian Arctic. *Nature Climate Change*, 11, 1–7. doi:  
944 10.1038/s41558-021-01087-6
- 945 Oprea, S., Martinez-Gonzalez, P., Garcia-Garcia, A., Castro-Vargas, J. A., Orts-  
946 Escolano, S., Garcia-Rodriguez, J., & Argyros, A. (2022, June). A Review  
947 on Deep Learning Techniques for Video Prediction. *IEEE Transactions on*  
948 *Pattern Analysis and Machine Intelligence*, 44(6), 2806–2826. (Conference  
949 Name: IEEE Transactions on Pattern Analysis and Machine Intelligence) doi:  
950 10.1109/TPAMI.2020.3045007
- 951 Petty, A. A., Schröder, D., Stroeve, J. C., Markus, T., Miller, J., Kurtz,  
952 N. T., ... Flocco, D. (2017). Skillful spring forecasts of Septem-  
953 ber Arctic sea ice extent using passive microwave sea ice observations.  
954 *Earth's Future*, 5(2), 254–263. Retrieved 2023-10-02, from [https://](https://onlinelibrary.wiley.com/doi/abs/10.1002/2016EF000495)  
955 [onlinelibrary.wiley.com/doi/abs/10.1002/2016EF000495](https://onlinelibrary.wiley.com/doi/abs/10.1002/2016EF000495) (\_eprint:  
956 <https://onlinelibrary.wiley.com/doi/pdf/10.1002/2016EF000495>) doi:  
957 10.1002/2016EF000495
- 958 Pfaff, T., Fortunato, M., Sanchez-Gonzalez, A., & Battaglia, P. (2020, October).  
959 Learning Mesh-Based Simulation with Graph Networks.. Retrieved 2023-11-09,  
960 from [https://openreview.net/forum?id=roNqYLO\\_XP](https://openreview.net/forum?id=roNqYLO_XP)

- 961 Pfeifer, P. E., & Deutsch, S. J. (1980). A STARIMA Model-Building Procedure with  
962 Application to Description and Regional Forecasting. *Transactions of the In-*  
963 *stitute of British Geographers*, 5(3), 330. Retrieved 2023-11-21, from [https://](https://www.jstor.org/stable/621846?origin=crossref)  
964 [www.jstor.org/stable/621846?origin=crossref](https://www.jstor.org/stable/621846?origin=crossref) doi: 10.2307/621846
- 965 Post, E., Bhatt, U. S., Bitz, C. M., Brodie, J. F., Fulton, T. L., Hebblewhite,  
966 M., ... Walker, D. A. (2013, August). Ecological Consequences of  
967 Sea-Ice Decline. *Science*, 341(6145), 519–524. Retrieved 2022-04-18,  
968 from <https://www.science.org/doi/full/10.1126/science.1235225>  
969 (Publisher: American Association for the Advancement of Science) doi:  
970 10.1126/science.1235225
- 971 Rubanova, Y., Sanchez-Gonzalez, A., Pfaff, T., & Battaglia, P. (2022, June).  
972 Constraint-based graph network simulator. In *Proceedings of the 39th Interna-*  
973 *tional Conference on Machine Learning* (pp. 18844–18870). PMLR. Retrieved  
974 2023-11-09, from <https://proceedings.mlr.press/v162/rubanova22a.html>  
975 (ISSN: 2640-3498)
- 976 Sanchez-Gonzalez, A., Godwin, J., Pfaff, T., Ying, R., Leskovec, J., & Battaglia,  
977 P. (2020, November). Learning to Simulate Complex Physics with Graph  
978 Networks. In *Proceedings of the 37th International Conference on Ma-*  
979 *chine Learning* (pp. 8459–8468). PMLR. Retrieved 2023-11-09, from  
980 <https://proceedings.mlr.press/v119/sanchez-gonzalez20a.html> (ISSN:  
981 2640-3498)
- 982 Seo, Y., Defferrard, M., Vandergheynst, P., & Bresson, X. (2018). Structured  
983 Sequence Modeling with Graph Convolutional Recurrent Networks. In  
984 L. Cheng, A. C. S. Leung, & S. Ozawa (Eds.), *Neural Information Pro-*  
985 *cessing* (pp. 362–373). Cham: Springer International Publishing. doi:  
986 10.1007/978-3-030-04167-0\_33
- 987 Serreze, M. C., & Meier, W. N. (2019). The Arctic’s sea ice cover: trends, vari-  
988 ability, predictability, and comparisons to the Antarctic. *Annals of the*  
989 *New York Academy of Sciences*, 1436(1), 36–53. Retrieved 2023-11-28,  
990 from <https://onlinelibrary.wiley.com/doi/abs/10.1111/nyas.13856>  
991 (\_eprint: <https://onlinelibrary.wiley.com/doi/pdf/10.1111/nyas.13856>) doi:  
992 10.1111/nyas.13856
- 993 Shi, X., Chen, Z., Wang, H., Yeung, D.-Y., Wong, W.-k., & WOO, W.-c.

- 1094 (2015). Convolutional LSTM Network: A Machine Learning Approach  
 1095 for Precipitation Nowcasting. In *Advances in Neural Information Pro-*  
 1096 *cessing Systems* (Vol. 28). Curran Associates, Inc. Retrieved 2023-  
 1097 11-09, from [https://proceedings.neurips.cc/paper/2015/hash/](https://proceedings.neurips.cc/paper/2015/hash/07563a3fe3bbe7e3ba84431ad9d055af-Abstract.html)  
 1098 [07563a3fe3bbe7e3ba84431ad9d055af-Abstract.html](https://proceedings.neurips.cc/paper/2015/hash/07563a3fe3bbe7e3ba84431ad9d055af-Abstract.html)
- 1099 Shi, Y., Huang, Z., Feng, S., Zhong, H., Wang, W., & Sun, Y. (2021, August).  
 1100 Masked Label Prediction: Unified Message Passing Model for Semi-Supervised  
 1101 Classification. In *Proceedings of the Thirtieth International Joint Confer-*  
 1102 *ence on Artificial Intelligence* (pp. 1548–1554). Montreal, Canada: Interna-  
 1103 tional Joint Conferences on Artificial Intelligence Organization. Retrieved  
 1104 2023-05-01, from <https://www.ijcai.org/proceedings/2021/214> doi:  
 1105 10.24963/ijcai.2021/214
- 1106 Sims, C. A. (1980). Macroeconomics and Reality. *Econometrica*, *48*(1), 1–48.  
 1107 Retrieved 2023-11-16, from <https://www.jstor.org/stable/1912017> (Pub-  
 1108 lisher: [Wiley, Econometric Society]) doi: 10.2307/1912017
- 1109 Srivastava, N., Mansimov, E., & Salakhudinov, R. (2015, June). Unsuper-  
 1110 vised Learning of Video Representations using LSTMs. In *Proceedings*  
 1111 *of the 32nd International Conference on Machine Learning* (pp. 843–852).  
 1112 PMLR. Retrieved 2023-11-09, from [https://proceedings.mlr.press/v37/](https://proceedings.mlr.press/v37/srivastava15.html)  
 1113 [srivastava15.html](https://proceedings.mlr.press/v37/srivastava15.html) (ISSN: 1938-7228)
- 1114 Stammerjohn, S. E., Drinkwater, M. R., Smith, R. C., & Liu, X. (2003).  
 1115 Ice-atmosphere interactions during sea-ice advance and retreat in the  
 1116 western Antarctic Peninsula region. *Journal of Geophysical Re-*  
 1117 *search: Oceans*, *108*(C10). Retrieved 2023-09-14, from [https://](https://onlinelibrary.wiley.com/doi/abs/10.1029/2002JC001543)  
 1118 [onlinelibrary.wiley.com/doi/abs/10.1029/2002JC001543](https://onlinelibrary.wiley.com/doi/abs/10.1029/2002JC001543) (\_eprint:  
 1119 <https://onlinelibrary.wiley.com/doi/pdf/10.1029/2002JC001543>) doi:  
 1120 10.1029/2002JC001543
- 1121 Stroeve, J., & Notz, D. (2018, September). Changing state of Arctic sea ice across  
 1122 all seasons. *Environmental Research Letters*, *13*(10), 103001. Retrieved 2023-  
 1123 11-28, from <https://dx.doi.org/10.1088/1748-9326/aade56> (Publisher:  
 1124 IOP Publishing) doi: 10.1088/1748-9326/aade56
- 1125 Stroeve, J. C., Serreze, M. C., Holland, M. M., Kay, J. E., Malanik, J., & Bar-  
 1126 rett, A. P. (2012, February). The Arctic’s rapidly shrinking sea ice cover:

- 1027 a research synthesis. *Climatic Change*, 110(3), 1005–1027. Retrieved  
 1028 2022-04-18, from <https://doi.org/10.1007/s10584-011-0101-1> doi:  
 1029 10.1007/s10584-011-0101-1
- 1030 Vihma, T. (2014, September). Effects of Arctic Sea Ice Decline on Weather and Cli-  
 1031 mate: A Review. *Surveys in Geophysics*, 35(5), 1175–1214. Retrieved 2023-  
 1032 02-09, from <https://doi.org/10.1007/s10712-014-9284-0> doi: 10.1007/  
 1033 s10712-014-9284-0
- 1034 Vitart, F., & Robertson, A. W. (2018, March). The sub-seasonal to seasonal  
 1035 prediction project (S2S) and the prediction of extreme events. *npj Cli-  
 1036 mate and Atmospheric Science*, 1(1), 1–7. Retrieved 2023-07-28, from  
 1037 <https://www.nature.com/articles/s41612-018-0013-0> (Number: 1  
 1038 Publisher: Nature Publishing Group) doi: 10.1038/s41612-018-0013-0
- 1039 Wang, C., Graham, R. M., Wang, K., Gerland, S., & Granskog, M. A. (2019, June).  
 1040 Comparison of ERA5 and ERA-Interim near-surface air temperature, snow-  
 1041 fall and precipitation over Arctic sea ice: effects on sea ice thermodynamics  
 1042 and evolution. *The Cryosphere*, 13(6), 1661–1679. Retrieved 2023-09-14,  
 1043 from <https://tc.copernicus.org/articles/13/1661/2019/> (Publisher:  
 1044 Copernicus GmbH) doi: 10.5194/tc-13-1661-2019
- 1045 Wu, Z., Jain, P., Wright, M. A., Mirhoseini, A., Gonzalez, J. E., & Stoica, I. (2022,  
 1046 January). *Representing Long-Range Context for Graph Neural Networks with  
 1047 Global Attention*. arXiv. Retrieved 2023-09-28, from [http://arxiv.org/abs/  
 1048 2201.08821](http://arxiv.org/abs/2201.08821) (arXiv:2201.08821 [cs])
- 1049 Yao, T., Tang, C. L., & Peterson, I. K. (2000). Modeling the seasonal vari-  
 1050 ation of sea ice in the Labrador Sea with a coupled multicategory ice  
 1051 model and the Princeton ocean model. *Journal of Geophysical Research:  
 1052 Oceans*, 105(C1), 1153–1165. Retrieved 2023-09-14, from [https://  
 1053 onlinelibrary.wiley.com/doi/abs/10.1029/1999JC900264](https://onlinelibrary.wiley.com/doi/abs/10.1029/1999JC900264) (\_eprint:  
 1054 <https://onlinelibrary.wiley.com/doi/pdf/10.1029/1999JC900264>) doi:  
 1055 10.1029/1999JC900264
- 1056 Yu, F., & Koltun, V. (2016, April). *Multi-Scale Context Aggregation by Dilated Con-  
 1057 volutions*. arXiv. Retrieved 2023-11-16, from [http://arxiv.org/abs/1511  
 1058 .07122](http://arxiv.org/abs/1511.07122) (arXiv:1511.07122 [cs]) doi: 10.48550/arXiv.1511.07122
- 1059 Zhang, J., & Rothrock, D. (2003, May). Modeling Global Sea Ice with a Thick-

1060           ness and Enthalpy Distribution Model in Generalized Curvilinear Coor-  
1061           dinates.       *Monthly Weather Review - MON WEATHER REV*, 131.       doi:  
1062           10.1175/1520-0493(2003)131<0845:MGSIWA>2.0.CO;2

1063       Zhang, M., Cui, Z., Neumann, M., & Chen, Y.       (2018, April).       An End-to-End  
1064       Deep Learning Architecture for Graph Classification.       *Proceedings of the*  
1065       *AAAI Conference on Artificial Intelligence*, 32(1).       Retrieved 2023-07-28,  
1066       from <https://ojs.aaai.org/index.php/AAAI/article/view/11782>       doi:  
1067       10.1609/aaai.v32i1.11782

Table 1: Selected input variables to the encoder, data source and rationale for inclusion.

<b>Short Name</b>	<b>Full Name</b>	<b>Source</b>	<b>Rationale for Inclusion</b>
sic	Sea ice concentration	GLORYS12	Direct measure of what is being forecasted; crucial for temporal dynamics and initial conditions.
sit	Sea ice thickness	GLORYS12	Provides insights into the resiliency and robustness of the ice, affecting its likelihood to melt or deform.
siuv	Sea ice velocities	GLORYS12	Indicates the direction and speed of sea ice movement.
so	Sea water salinity	GLORYS12	Salinity affects the freezing point of sea water and is crucial in the dynamics of ice formation and melt.
sst	Sea surface temperature	GLORYS12	The temperature of surrounding sea water directly affects ice melt and formation rates.
t2m	2-meter temperature	ERA5	Air temperature can provide additional context for the thermal conditions affecting the sea ice surface.
u10/v10	10-meter wind velocity	ERA5	Influences the motion and deformation of sea ice.
sshf	Surface sensible heat flux	ERA5	Surface sensible heat flux is an indicator of the heat exchange between the atmosphere and the sea surface, affecting ice melt and formation.
x	x-position of each node	—	Provides the latitudinal spatial context for each data point.
y	y-position of each node	—	Provides the longitudinal spatial context for each data point.
doy	Day of the year	—	Provides temporal context.
csize	Cell size	—	Provides the relative size of the area covered by each cell for additional spatial context.

Table 2: Summary of developed model configurations. The models differ in their spatial convolutions and their underlying meshes, with the aim of contrasting the attention-based transformer convolution with the graph convolutional network, as well as demonstrating the model’s ability to model over an irregular mesh.

<b>Name</b>	<b>Convolution (# stacked layers)</b>	<b>Mesh</b>	<b>Approximate training time</b>
<b>GraphSIFNet-Att</b>	TransformerConv (3)	Irregular ( $1/12^\circ$ - $1/3^\circ$ )	10h (30 epochs)
<b>GraphSIFNet-Att-Reg</b>	TransformerConv (3)	Regular ( $1/3^\circ$ )	8h (30 epochs)
<b>GraphSIFNet-GCN</b>	GCN (6)	Irregular ( $1/12^\circ$ - $1/3^\circ$ )	10h (45 epochs)
<b>Baseline</b>	N/A	N/A	N/A